fluids

MDPI

Article

Experimental and Numerical Investigation of an Integrated Fan-Driven Co-Flow Jet System for a High-Performance Automotive Rear Wing

Marco Robert Herberg [1,*], Guglielmo Luca Bambino [1], Stefano De Pinto [1], Giuseppe Pascazio [2] and Marco Donato de Tullio [2]

[1] McLaren Automotive Europe SL, 43710 Santa Oliva, Spain; guglielmoluca.bambin@mclaren.com (G.L.B.); stefano.depinto@mclaren.com (S.D.P.)
[2] Department of Mechanics, Mathematics and Management, Politecnico di Bari, 70125 Bari, Italy; giuseppe.pascazio@poliba.it (G.P.); marcodonato.detullio@poliba.it (M.D.d.T.)
* Correspondence: marcorobert.herberg@poliba.it

Abstract

This study investigates the application of the Co-Flow Jet (CFJ) active flow-control methodology to an automotive rear wing through a combined CFD and experimental campaign conducted on a modified McLaren 765LT. The work evaluates the aerodynamic response, energy performance, and practical integration of embedded Co-Flow systems under representative on-track conditions. An extensive CFD design campaign assessed multiple Co-Flow architectures, from which three representative configurations incorporating embedded ducted axial fans were selected for experimental testing. The results indicate that aerodynamic performance is strongly influenced by the interaction between momentum injection, vehicle conditions, and duct architecture. The most effective configuration achieved drag reductions of up to 9% together with downforce increases of approximately 15% under highly loaded conditions, significantly exceeding the repeatability levels of the measurements. The efficiency analysis further showed that, under selected operating conditions, the aerodynamic benefits obtained from the Co-Flow system can exceed the electrical power required by the actuation system. However, increased mass-flow capability alone was not found to guarantee improved aerodynamic performance or efficiency. The results demonstrate the successful integration and operation of a fan-driven Co-Flow system on a production-based vehicle and highlight the importance of momentum injection level and duct design. The findings should be interpreted within the scope of the investigated vehicle and operating envelope. Due to confidentiality constraints, part of the absolute aerodynamic data could not be disclosed, and the results are therefore presented primarily as relative variations.

Keywords: Co-Flow Jet; active flow control; boundary-layer energization; drag reduction; rear wing aerodynamics; RANS CFD; experimental validation; aerodynamic efficiency; flow separation control; high-performance automotive

Check for updates

Academic Editor: Ivette Rodriguez

Received: 17 May 2026
Revised: 16 June 2026
Accepted: 17 June 2026
Published: 22 June 2026

Copyright: © 2026 by the authors. Licensee MDPI, Basel, Switzerland. This article is an open access article distributed under the terms and conditions of the Creative Commons Attribution (CC BY) license.

1. Introduction

Aerodynamic optimization plays a fundamental role in modern vehicle design, where drag reduction and downforce generation often represent competing objectives [1,2]. In passenger and high-performance vehicles, aerodynamic performance directly influences

fuel consumption, vehicle stability, top speed, braking performance, and cornering capability [2,3]. Significant research efforts have been devoted to the development of aerodynamic devices and flow-management strategies capable of improving vehicle efficiency while satisfying increasingly demanding performance, sustainability, and regulatory requirements [1,4,5]. Recent numerical and experimental investigations have further demonstrated the effectiveness of aerodynamic optimization strategies based on external-flow management, rear aerodynamic devices, and CFD-driven design methodologies for enhancing vehicle performance and efficiency under realistic operating conditions [6,7]. Over the last decades, substantial aerodynamic improvements have been achieved through passive solutions such as optimized body shaping, diffusers, vortex generators, spoilers, underbody treatments, and wake-management devices [1,4,5]. These solutions remain attractive due to their simplicity, robustness, and absence of additional energy requirements during operation. Their effectiveness is often restricted to relatively narrow operating conditions and may involve compromises between drag reduction, aerodynamic loading, manufacturability, and vehicle integration [1,4,8]. These limitations, combined with the growing need for adaptive aerodynamic performance, have stimulated considerable interest in active aerodynamic technologies capable of responding dynamically to changing operating conditions. Among these technologies, Active Flow Control (AFC) methodologies employ external actuation to modify boundary-layer development, delay flow separation, alter wake structures, and improve aerodynamic performance [8–10]. AFC techniques have been investigated for a wide range of automotive applications, including drag reduction, wake control, aerodynamic load management, and vehicle stability enhancement [8,11,12]. Recent reviews have highlighted that the practical implementation of automotive AFC systems depends not only on aerodynamic effectiveness but also on factors such as energy consumption, packaging constraints, system integration, reliability, scalability, and overall vehicle-level efficiency [1,8,11,12]. Among the various AFC approaches, fluidic actuation techniques have attracted significant attention because they can influence the flow field without requiring large-scale moving aerodynamic surfaces. Steady blowing and suction systems, synthetic jets, plasma actuators, morphing concepts, and hybrid flow-control strategies have all demonstrated the capability to modify boundary-layer development, alter wake structures, and reduce aerodynamic losses under both laboratory and realistic operating conditions [10,13–17]. Current research is therefore increasingly focused on balancing aerodynamic gains against the energetic and practical costs associated with flow-control actuation [1,8,11,13]. To investigate aerodynamic control strategies under controlled conditions, simplified bluff-body configurations are frequently employed as benchmark geometries. Among these, the Ahmed body introduced by Ahmed et al. [18] remains one of the most widely adopted reference models for studying flow separation, wake development, and pressure-drag generation in road vehicles. Numerous experimental and numerical investigations have subsequently employed Ahmed-type configurations to assess both passive and active drag-reduction methodologies, providing valuable insight into the physical mechanisms governing wake dynamics and aerodynamic losses [19–23]. In particular, several studies have investigated active flow-control concepts based on steady blowing, suction, synthetic jets, and combined actuation techniques, often reporting significant drag reductions under highly separated flow conditions [15,16,20–22]. These investigations have substantially improved the understanding of aerodynamic drag-reduction mechanisms and wake manipulation strategies applicable to automotive flows. Within this context, increasing attention has recently been devoted to the Co-Flow Jet (CFJ) methodology, originally developed for aerospace applications [24–27]. The CFJ concept combines tangential blowing and downstream suction to create a recirculating flow-control system characterized by approximately zero-net mass flux. By simultaneously energizing the boundary layer

and removing low-momentum fluid, CFJ actuation can delay flow separation, improve pressure recovery, and enhance aerodynamic efficiency under strong adverse pressure gradients. Previous numerical and experimental investigations conducted on airfoils, high-lift systems, and simplified automotive configurations have demonstrated substantial improvements in aerodynamic performance through appropriate momentum injection and suction balancing [28–31]. More recently, CFJ methodologies have also been investigated for bluff-body automotive applications. Derghal et al. [32] reported drag reductions of approximately 7% on an Ahmed body through coupled blowing and suction slots arranged along the rear slant, highlighting the strong sensitivity of the control effectiveness to slot positioning and jet momentum. Similarly, Jahanmiri et al. [33] experimentally demonstrated drag reductions of approximately 4% using combined suction and base blowing, emphasizing the importance of properly balancing injected and extracted mass flow rates. Unlike these studies, the present work employs experimentally characterized fan hardware and evaluates the coupled interaction between aerodynamic loading, fan operating characteristics, and actuation-system performance under realistic vehicle-integration constraints. Although previous CFJ investigations have reported encouraging results, most available studies remain focused on simplified aerodynamic configurations and idealized actuation strategies. Ahmed-body investigations have significantly advanced the understanding of drag-reduction mechanisms associated with blowing and suction actuation; however, they do not fully capture the aerodynamic complexity of production-scale vehicle components, where strong three-dimensional interactions, geometric constraints, structural requirements, and packaging limitations can substantially influence flow-control effectiveness. Another important limitation is that blowing and suction are commonly prescribed directly as boundary conditions. Such an approach neglects the influence of realistic actuation hardware, fan operating characteristics, duct losses, and electrical-power requirements, all of which may strongly affect the achievable aerodynamic benefit. As a result, the relationship between aerodynamic performance, actuation-system behaviour, and energetic cost remains insufficiently understood, particularly in automotive applications where installation volume and onboard power are inherently constrained. This situation raises an important unresolved question: can the aerodynamic benefits observed in idealized CFJ studies be maintained when the system is integrated into a realistic automotive architecture subject to practical geometric, energetic, and packaging constraints? Addressing this challenge requires moving beyond simplified laboratory configurations and evaluating the coupled interaction between aerodynamic loading, actuation-system behaviour, and vehicle-scale flow structures. The present work addresses this challenge through a combined numerical and experimental investigation of an embedded fan-driven Co-Flow Jet system integrated within the rear wing of a full-scale high-performance vehicle. The novelty of the study does not reside in the Co-Flow Jet concept itself, which has already been extensively investigated in the literature, but rather in its implementation under realistic automotive constraints. The primary contribution is the integration of experimentally characterized fan hardware, duct-design constraints, full-vehicle CFD simulations, and full-scale experimental testing within a unified framework that explicitly accounts for the interaction between aerodynamic loading, fan operating characteristics, and system-level power requirements. By combining these elements, the study provides a realistic assessment of CFJ feasibility and effectiveness in an automotive application, helping to bridge the gap between idealized flow-control investigations and practical vehicle integration.

More specifically, the present study contributes:

- A CFD-based design and optimization campaign involving multiple Co-Flow architectures;
- The integration of experimentally characterized ducted-fan actuation within a production-based rear-wing assembly;

- Full-scale experimental assessment of aerodynamic performance, pressure distributions, and energy consumption under representative on-track operating conditions;
- A combined evaluation of aerodynamic effectiveness and energy efficiency using experimentally measured actuation-system characteristics.

The present work focuses on establishing the aerodynamic effectiveness and practical viability of the proposed architecture, providing a foundation for future studies aimed at the detailed characterization of the underlying flow structures and the optimization of the system through advanced experimental diagnostics, including particle image velocimetry (PIV), wake-rake surveys, and velocity-field measurements.

2. Baseline Vehicle Characterization

The aerodynamic baseline of the investigated vehicle was characterized through a combined numerical and experimental approach. This section describes the CFD methodology, experimental setup, and validation procedures used to establish the reference framework for the subsequent Co-Flow investigations. Throughout this work, aerodynamic quantities are evaluated at either vehicle or wing level depending on the purpose of the analysis. During the CFD-based design and optimization process, rear-wing aerodynamic quantities, including $C_{d,wing}$, $C_{l,wing}$, and the pressure-coefficient distribution (C_p), are primarily used to compare and rank candidate Co-Flow architectures. Although the CFD simulations are performed on the complete vehicle geometry, the aerodynamic assessment focuses on the rear-wing response to support the selection of the most promising duct configurations. For the experimental assessment, vehicle-level quantities are employed. The drag coefficient $C_{d,veh}$ and lift coefficient $C_{d,veh}$ are used to quantify the aerodynamic behaviour of the vehicle and to evaluate the effect of the selected Co-Flow systems under full-scale operating conditions. The pressure coefficient (C_p) is treated separately as a local aerodynamic quantity measured on the rear-wing surface and compared with the corresponding CFD predictions. Together, these global and local aerodynamic metrics provide the basis for the numerical and experimental investigations presented in the following chapters.

2.1. CFD Setup

Numerical simulations were performed using Simcenter STAR-CCM+ by solving the steady Reynolds-Averaged Navier–Stokes (RANS) equations. The CFD methodology was intended to support the evaluation and optimization of multiple Co-Flow Jet configurations rather than to resolve all turbulent flow structures associated with large-scale separation phenomena. The simulations employed the Realizable k–ε turbulence model in combination with the Two-Layer All y^+ wall-treatment approach. This modelling strategy was selected as a compromise between computational efficiency, numerical robustness, and consistency with the industrial aerodynamic-development methodology routinely adopted across related vehicle-development projects. The use of a common modelling framework enabled the investigation of a large number of candidate configurations while maintaining a consistent basis for comparison. Due to the geometric symmetry of the vehicle, only half of the model was simulated, reducing computational cost while preserving the dominant aerodynamic features (Figure 1). The computational domain was defined to ensure adequate development of the external flow field and wake structures while maintaining a computational cost compatible with the large number of configurations investigated during the design campaign. A symmetry (slip-wall) boundary condition was applied at the longitudinal center plane. A moving ground plane and rotating wheels were employed to reproduce the relative motion between the vehicle and the road surface, while no-slip wall conditions were imposed on all vehicle surfaces. Convergence was assumed when the

monitored aerodynamic coefficients remained effectively constant over successive iterations and the residuals stabilized at values of the order of 10^{-4} or lower.

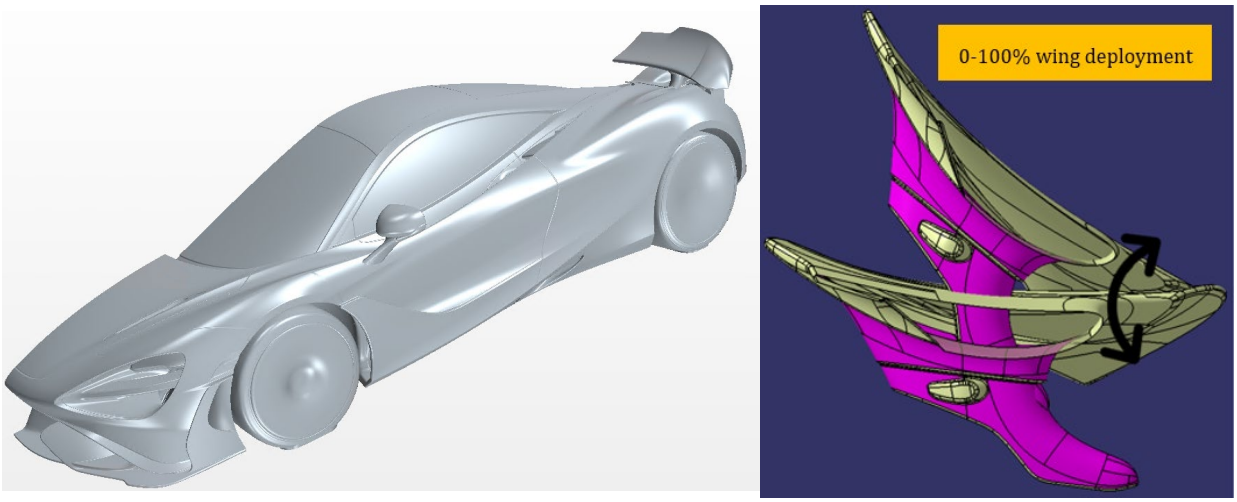


Figure 1. Half–vehicle CFD model of the McLaren 765LT and investigated rear-wing deployment range (0–100%). The rear wing was used as the primary aerodynamic device for the implementation and assessment of the Co-Flow configurations.

The authors acknowledge that higher-fidelity turbulence-modelling approaches, such as SST k–ω, DES, IDDES, or LES, may provide improved prediction of boundary-layer development, separation onset, and wake dynamics. Previous investigations have demonstrated that turbulence-model selection can influence the prediction of separated-flow structures in automotive applications characterized by strong adverse pressure gradients and complex three-dimensional flow features [34]. The objective of the present CFD campaign was not the absolute prediction of all separated-flow phenomena, but rather the identification and ranking of promising Co-Flow Jet configurations prior to experimental validation. For this reason, a turbulence-model sensitivity study was considered beyond the scope of the present work. All simulations were performed using a consistent computational domain, boundary conditions, meshing strategy, and solver settings throughout the investigation, ensuring the consistency of the comparative analysis. Local mesh refinements were applied in the vicinity of the rear-wing assembly to ensure adequate resolution of the aerodynamic loads and pressure distributions used throughout the study. The full-vehicle computational mesh consisted of more than 120 million cells and employed a polyhedral discretization combined with prism-layer refinement in proximity to solid surfaces. A total of 15 prism layers were adopted, with a first-cell height of approximately 0.055 mm, a total prism-layer thickness of 4 mm, and a growth rate of 1.2. Dedicated local mesh refinements were applied in the vicinity of the rear wing and Co-Flow Jet system, resulting in wall y^+ values below 10 over the aerodynamic surfaces directly affected by the actuation mechanism. Mesh-quality diagnostics confirmed a topologically valid mesh with no negative-volume cells, a minimum face validity of 0.98, a minimum cell quality of 0.015, and a maximum skewness angle of less than 80° within the refined rear-wing region. Although the full-vehicle mesh topology and specific vehicle geometric features cannot be disclosed due to industrial confidentiality constraints, the robustness and consistency of the numerical methodology were verified through a representative mesh-sensitivity study conducted on an isolated baseline rear-wing model (Figure 2). This assessment was conducted to quantify the sensitivity of the aerodynamic response to spatial discretization and to identify a mesh resolution ensuring numerical consistency of the governing flow quantities within the boundary layer and near-wake regions. The rear wing was selected as

the reference configuration for mesh assessment because it contains the dominant flow features governing its aerodynamic performance, including strong adverse pressure gradients, boundary-layer development, and wake formation. These features are locally sensitive to mesh resolution and provide a suitable basis for evaluating discretization effects in the regions of interest. The mesh refinement results showed that variations in lift and drag coefficients decreased to below 1.5% and 1.0%, respectively, between the two finest mesh levels, indicating satisfactory numerical convergence for the purpose of comparative analysis. The resulting mesh resolution, including a near-wall target resolution of $y^+ \approx 1$, was subsequently adopted for all full-vehicle simulations to ensure a consistent discretization strategy across all investigated configurations. The mesh-sensitivity study was not intended to achieve a fully asymptotic mesh-independent solution of the complete vehicle, but to ensure that the aerodynamic quantities used for configuration ranking were not sensitive to further mesh refinement within the investigated range. This approach is consistent with the use of the CFD model as a comparative design-support tool prior to experimental validation. To reduce computational cost during the grid-convergence assessment, the isolated rear-wing model employed a coarser near-wall resolution, resulting in representative wall y^+ values in the range of approximately 40–60. This choice remained compatible with the adopted Two-Layer All y^+ wall-treatment approach and was considered adequate for evaluating the influence of mesh density on the aerodynamic loads and pressure distributions governing the design-selection process.

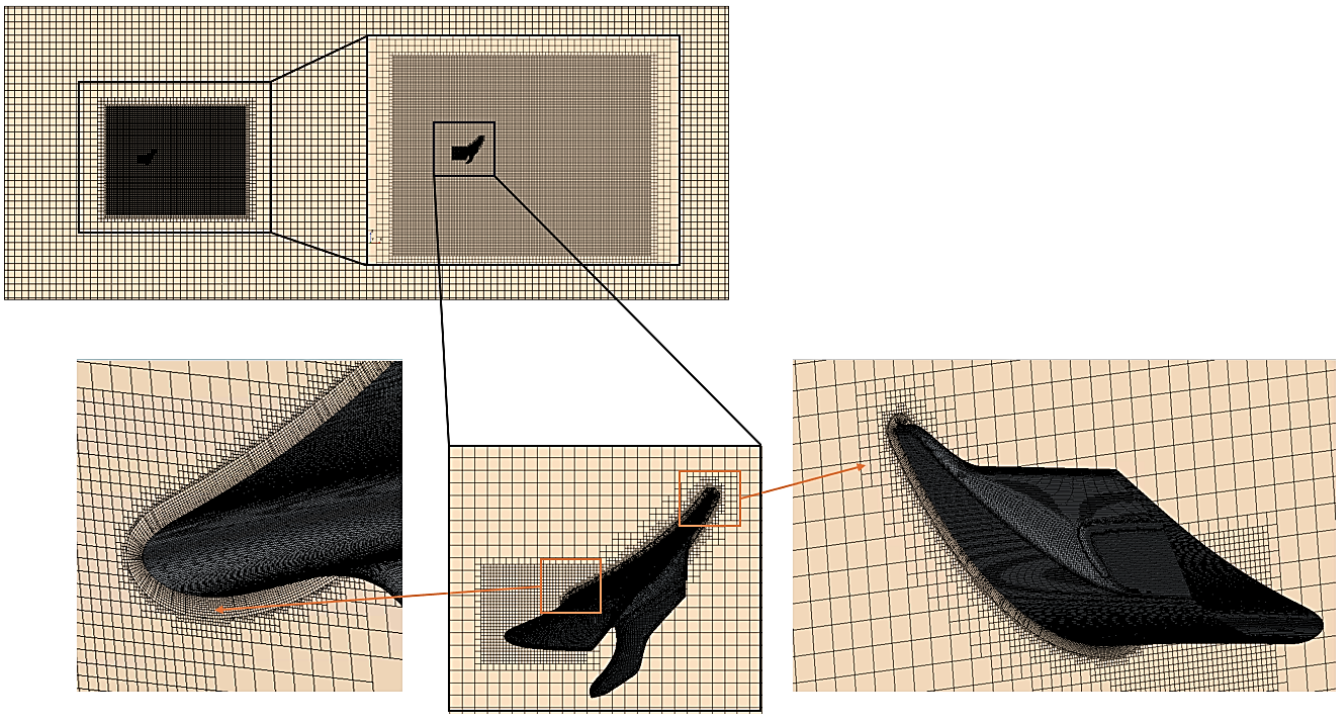


Figure 2. Computational mesh adopted for the CFD simulations, showing local refinement regions around the rear wing and near-wall prism-layer treatment used to resolve the boundary layer.

Simulations were performed under International Standard Atmosphere (ISA) conditions, assuming an air temperature of 288.15 K, a pressure of 101,325 Pa, and an air density of 1.225 kg/m^3.

The results showed negligible variations in the aerodynamic coefficients with increasing mesh density, confirming mesh independence of the numerical solution (Table 1).

Table 1. Mesh-sensitivity assessment performed on the isolated rear-wing configuration at 100% deployment. Variations are reported relative to the baseline mesh.

Wing %	Model	Mesh	$C_{l,wing}$	$C_{d,wing}$	Delta $C_{l,wing}$	Delta $C_{d,wing}$	Cells Count
100	k–ξ	Baseline	−0.3101	0.1035	–	–	6.16×10^6
100	k–ξ	Finer 1	−0.3074	0.1024	−0.85%	−0.99%	1.05×10^7
100	k–ξ	Finer 2	−0.3048	0.0997	−0.87%	−2.68%	2.09×10^7
100	k–ξ	Finer 3	−0.3005	0.0983	−1.40%	−1.41%	3.58×10^7

The interaction between the main wing and the supporting structure generates complex three-dimensional pressure gradients (Figure 3). The resulting flow field is illustrated through contours of skin-friction coefficient (C_f), pressure coefficient (C_p), and velocity magnitude. The C_f distribution highlights regions of strong shear near the leading edge and along the suction side, while localized reductions indicate areas susceptible to flow separation or adverse pressure gradients, particularly in the junction region.

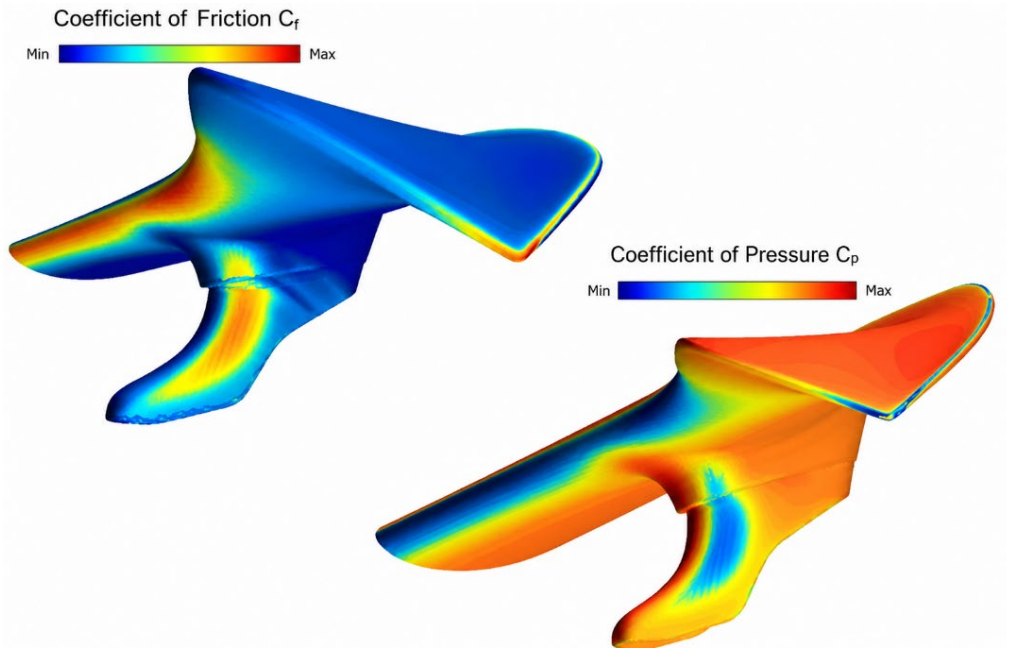


Figure 3. Representative CFD distributions of skin-friction coefficient (C_f) and pressure coefficient (C_p) on the isolated rear wing. The results illustrate the main flow-acceleration and pressure-loading regions governing aerodynamic performance.

The C_p contours reveal a pronounced suction peak on the leading edge, followed by a gradual pressure recovery toward the trailing edge, consistent with lifting aerodynamic behaviour. In Figure 4, the velocity field further confirms these features, showing acceleration over the suction surface and a well-defined wake downstream of the profile. Regions of low velocity and recirculation are observed in the near-wake and in the junction area, indicating potential sources of aerodynamic losses.

The CFD results capture the main flow features around the baseline vehicle and provide the reference framework for the subsequent Co-Flow analyses.

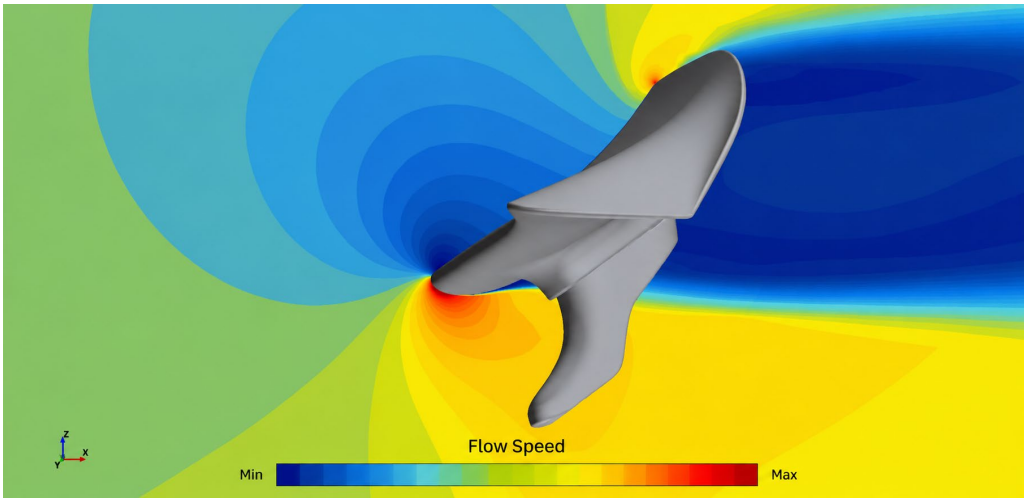


Figure 4. Velocity contours around the isolated rear-wing section. The accelerated flow over the suction side and the associated pressure gradients are clearly visible.

2.2. Vehicle Setup

The test vehicle was instrumented to simultaneously acquire aerodynamic and vehicle-dynamics quantities during on-track testing. The measured parameters included:

- Pressure coefficient distributions across nine spanwise sections of the rear wing, as defined in Figure 5.
- Aerodynamic drag, derived from coastdown tests using longitudinal acceleration measurements [35].
- Downforce, estimated from suspension displacement through calibrated correlation curves [35].

A total of 64 static pressure ports were installed on the suction-side only of the rear wing, matching the CFD pressure-tap locations to enable direct comparison between numerical and experimental C_p distributions. In the Co-Flow configurations, the internal ducting reduced the number of available probes to 46 while preserving the spanwise distribution (Figure 5).

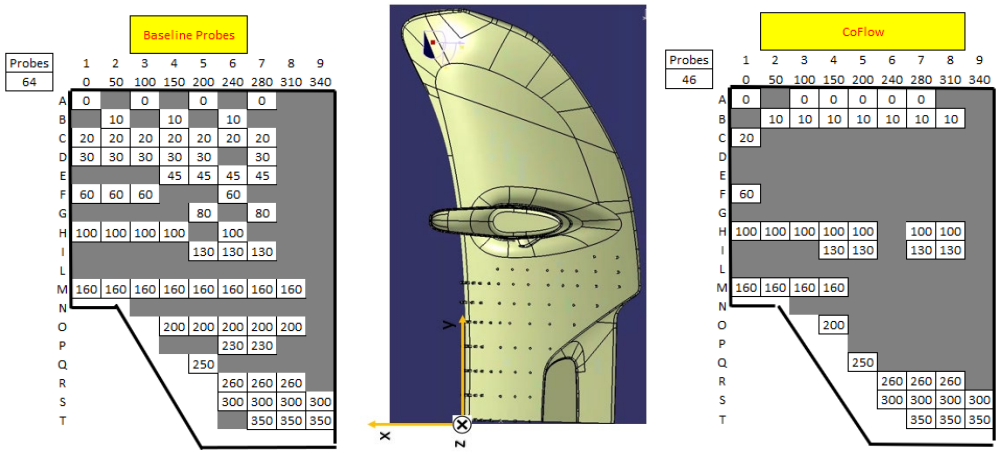


Figure 5. Static pressure measurement layout adopted for the experimental campaign. The central image shows the probe locations on the rear wing, while the left and right panels report the pressure-tap distributions for the baseline and Co-Flow configurations, respectively.

Due to budget constraints, wind tunnel testing was not performed; instead, experiments were conducted at the Idiada Applus+ Proving Ground, using a high-speed track

featuring two 2 km straights. Both steady-state and coastdown tests were carried out. For drag estimation, a Racelogic VBox II system was used to accurately measure vehicle speed and deceleration. The freestream reference pressure was measured using a Pitot tube mounted on the front bonnet and connected to a differential-pressure sensor acquired through an Arduino R4 data-acquisition system. Due to the installation geometry, the Pitot probe (Figure 6) operated with an inclination of approximately 5° relative to the main flow stream. Although this configuration may introduce a systematic bias in the measured total pressure, the effect was estimated to remain below 1% of the dynamic pressure and was considered constant across all tested configurations; therefore, it does not affect the comparative analyses presented in this work. Instrument uncertainties were estimated from manufacturer specifications and treated according to the GUM framework. These uncertainties were subsequently complemented by the repeatability analysis performed on six repeated runs for each operating condition as shown in Table 2. Data processing followed a standardized workflow, with all signals filtered using a moving-average approach to reduce high-frequency noise while preserving the underlying aerodynamic trends. Transient phases at the beginning of each run were excluded to ensure that only stabilized data were considered.

Table 2. Overview of measurement systems employed in the experimental setup and corresponding standard uncertainties. Uncertainty values are obtained from manufacturer specifications and reported as standard uncertainties following the GUM methodology.

Measurement	Instrument	Standard Uncertainty
Vehicle speed	Racelogic VBOX	0.016 m/s
Longitudinal acceleration	Racelogic VBOX	0.02 m/s^2
Pressure	McLaren PIN16	1.30 mbar
Differential pressure	Pitot transducer	0.13 mbar
Suspension displacement	Potentiometer	0.144 mm

Vehicle drag was estimated via the coastdown method in accordance with SAE J1263 [36], complemented by the Segers approach [35]; the latter is intended as a rapid tool for assessing trends in drag variation, rather than delivering absolute values, which would require a dedicated wind tunnel measurement campaign.



Figure 6. Experimental instrumentation used during vehicle testing, including the front-mounted Pitot probe for dynamic-pressure measurements and the rear-wing static-pressure acquisition system.

The coastdown method provides an estimation of the drag area $C_{d,veh} \times A$, from which the drag coefficient $C_{d,veh}$ can be derived assuming a reference area. Air density was computed from ambient pressure and temperature measurements, assuming ideal gas behaviour. At high vehicle speeds, aerodynamic drag dominates the total resistive forces, allowing the longitudinal acceleration signal to be primarily attributed to aerodynamic effects. Downforce was estimated from suspension displacement measurements using four rotary potentiometers installed at each suspension corner, again according to the Segers' method [35]. Suspension displacements were converted into vertical loads using calibration curves and kinematic relationships, enabling the estimation of aerodynamic downforce distribution across the vehicle. For steady-state tests, as per drag measurements, steering angle was required to remain within $\pm 2^{\circ}$ to avoid cornering effects, and vehicle speed stability was maintained within ± 1 km/h. Due to confidentiality restrictions imposed by McLaren Automotive Ltd., some quantitative data are presented in normalized form or without explicit numerical values. Even so, the reported trends remain fully representative of the underlying aerodynamic behaviour and enable consistent comparison between the baseline and Co-Flow configurations.

2.3. Baseline CFD vs. Experimental Results

To assess the reliability of the adopted numerical methodology, CFD predictions were compared against full-scale experimental measurements acquired on the baseline vehicle.

2.3.1. C_d Comparison

Before discussing the CFD-to-experiment correlation, the repeatability of the experimental vehicle drag measurements was assessed. Table 3 reports the coefficient of variation in the measured drag-coefficient values for the baseline vehicle across the investigated airbrake deployment conditions calculated as follows:

$$CV(C_{d,veh})[\%] = \frac{\sigma_{C_d}}{\mu_{C_d}} \times 100 \quad (1)$$

where σ_{C_d} is the standard deviation of each set of experimental drag-coefficient measurements and μ_{C_d} is the corresponding mean value. The resulting coefficients of variation remained relatively small throughout the test campaign, indicating good consistency of the acquisition chain and experimental procedure. A global repeatability assessment yielded an average CV of the coefficient of drag of 1.89%, with a standard deviation of 0.68%, confirming the stability and robustness of the measurement methodology.

In addition to repeatability, the uncertainty associated with the drag estimation procedure was evaluated through uncertainty propagation according to the Guide to the Expression of Uncertainty in Measurement (GUM) methodology. The uncertainty analysis considers the dominant measurement quantities directly involved in the drag-area calculation, namely longitudinal acceleration, vehicle speed, vehicle mass, and air-density determination. Additional sources of variability associated with road gradient and ambient wind conditions were mitigated through the experimental procedure. In particular, coastdown tests were performed in both driving directions and only under environmental conditions compliant with the SAE J1263 recommendations, with ambient wind speeds below 2 m/s. The residual influence of these factors is therefore reflected in the repeatability statistics obtained from the repeated measurements rather than in the analytical uncertainty propagation. The uncertainty associated with the drag estimation was evaluated through uncertainty propagation of the coastdown formulation, considering the contributions of vehicle acceleration, velocity measurement, air-density estimation, and vehicle mass. The dominant contributions were associated with acceleration measurement and air-density

estimation, while vehicle-mass uncertainty was found to be negligible. The resulting expanded uncertainty was estimated to be approximately 6% (k = 2, 95% confidence). The resulting experimental drag values were subsequently compared with the CFD predictions, as shown in Figure 7. The comparison showed good agreement in terms of global drag trends across the investigated operating conditions. At lower rear-wing deployment levels, CFD simulations slightly overpredicted the aerodynamic drag relative to the experimental measurements, whereas at higher deployment conditions, the trend progressively reversed and the experimentally measured drag became higher than the numerical prediction. Despite these discrepancies, the differences remained within single-digit percentage values, confirming the suitability of the numerical model for comparative aerodynamic analyses.

Table 3. Repeatability assessment of baseline vehicle drag-coefficient measurements expressed through the coefficient of variation (CV). Global statistics are calculated considering all investigated wing-deployment conditions.

Airbrake Deployment [%]	CV($C_{d,veh}$) [%]
0%	1.41%
10%	1.24%
20%	1.22%
30%	1.69%
40%	2.87%
50%	1.28%
60%	2.52%
70%	1.99%
80%	1.19%
90%	2.56%
100%	2.81%
Global Repeatability Metrics	
CV($C_{d,veh}$) average [%]	1.89%
CV($C_{d,veh}$) Std. Dev. [%]	0.68%

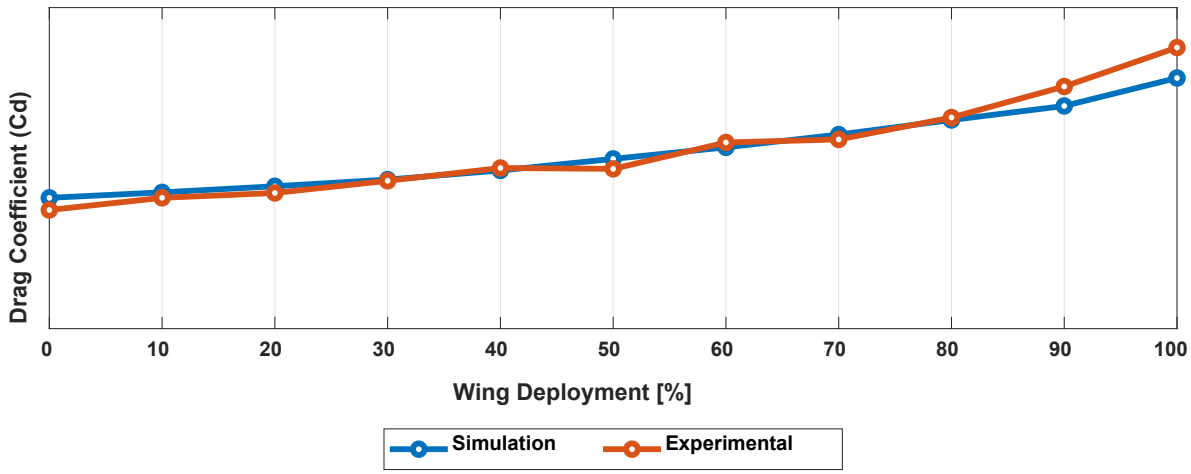


Figure 7. Comparison between CFD predictions and experimental measurements of the vehicle drag coefficient as a function of rear-wing deployment. The agreement supports the use of the CFD methodology as a comparative design-support tool.

Although absolute drag values cannot be disclosed due to confidentiality restrictions, the observed agreement between CFD predictions and experimental measurements, to-

gether with the demonstrated repeatability of the experimental methodology, provides confidence in the adopted approach and supports the use of the numerical model as a comparative design-support tool throughout the Co-Flow development process.

2.3.2. C_l Comparison

Prior to the CFD comparison, the repeatability of the experimentally estimated aerodynamic load was assessed across all investigated operating conditions. Table 4 reports the coefficient of variation ($CV(C_{l,veh})$) of the measured lift-coefficient values for the baseline vehicle across the investigated airbrake deployment conditions calculated as follows:

$$CV(C_{l,veh})[\%] = \frac{\sigma_{C_l}}{\mu_{C_l}} \times 100 \quad (2)$$

where σ_{C_l} is the standard deviation of each set of experimental lift-coefficient measurements and μ_{C_l} is the corresponding mean value. For the sake of clarity, only the results associated with the highest airbrake deployment levels (70–100%) are reported in Table 4. These operating conditions correspond to the largest aerodynamic loads and therefore represent the most relevant cases from both an experimental and aerodynamic perspective. The reported global repeatability metrics were nevertheless calculated considering the complete set of investigated operating conditions. The coefficient of variation (CV [%]) obtained from the repeated measurements remained relatively limited throughout the test matrix, with an average value of approximately 2.54% and a standard deviation of 1.64%, as shown in Table 4. The observed variability is higher than that reported for drag measurements, reflecting the indirect nature of the downforce evaluation procedure based on suspension-displacement measurements and calibration correlations. However, the results indicate an acceptable level of repeatability for comparative aerodynamic assessments.

As per drag measurements, the uncertainty associated with the aerodynamic load determination was evaluated through uncertainty propagation according to the Guide to the Expression of Uncertainty in Measurement (GUM) methodology. The uncertainty associated with the aerodynamic-load determination was evaluated considering the dominant quantities involved in the Segers methodology, namely suspension spring-rate tolerances, motion-ratio estimation, and displacement-sensor accuracy. The resulting expanded uncertainty was estimated to be approximately 10% (k = 2, 95% confidence). The resulting experimental lift-coefficient values were subsequently compared with the CFD predictions, as shown in Figure 8, only for the highest wing deployment values. A systematic overprediction of aerodynamic load was observed.

This behaviour is consistent with the known limitations of steady RANS methodologies when applied to highly loaded three-dimensional flows. As aerodynamic loading increases, the influence of localized separation and unsteady flow structures may become more significant. Under these conditions, the numerical model can predict a more attached flow field than that observed experimentally, leading to a moderate overestimation of aerodynamic load. Despite this systematic bias, the CFD simulations consistently reproduced the general aerodynamic trends and relative variations across the investigated operating conditions. The experimental measurements exhibited a variation of approximately eight percentage points across the investigated operating range. The CFD results reproduced both the magnitude and progression of the measured trend, supporting the use of the numerical methodology for comparative aerodynamic assessments. Considering experimental repeatability, the estimated uncertainty associated with the load determination methodology, and the complexity of the investigated flow field, the level of agreement obtained is considered satisfactory for comparative aerodynamic analyses and configuration assessment.

Table 4. Repeatability assessment of vehicle lift-coefficient measurements for all investigated operating conditions. The reported coefficient of variation (CV) quantifies the measurement dispersion obtained from repeated tests.

vVeh Adim	Airbrake [%]	CV($C_{l,veh}$) [%]
v1	70	2.22%
v1	80	6.60%
v1	90	2.51%
v1	100	1.10%
v2	70	4.06%
v2	80	2.47%
v2	90	1.66%
v2	100	0.34%
v3	70	2.31%
v3	80	5.12%
v3	90	2.50%
v3	100	3.82%
v4	70	2.09%
v4	80	0.87%
v4	90	1.07%
v4	100	1.90%
Global Repeatability Metrics		
CV($C_{l,veh}$) average variation [%]	2.54%	
CV($C_{l,veh}$) Std. Dev. [%]	1.64%	

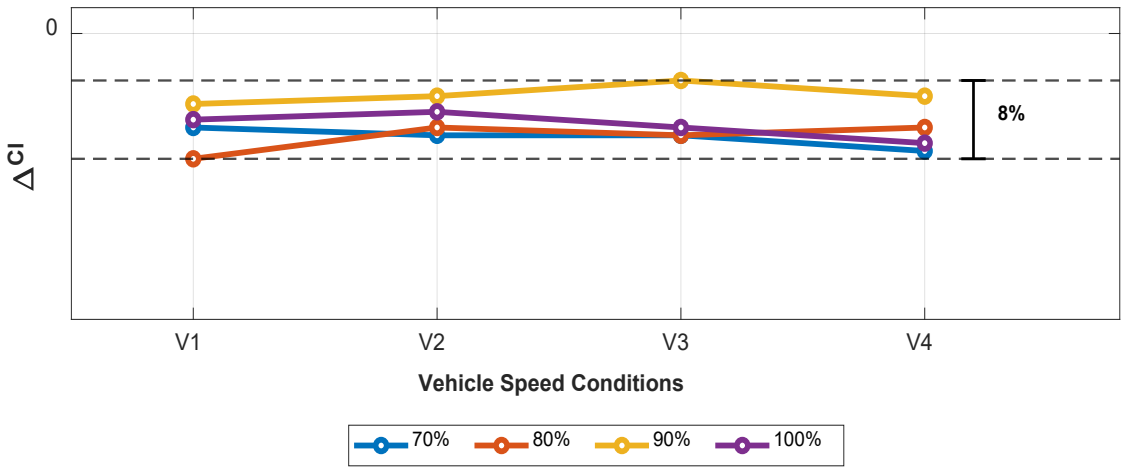


Figure 8. Comparison between CFD and experimental trends of rear-wing lift coefficient under high-load operating conditions (70–100% wing deployment, v1–v4).

2.3.3. C_p Comparison

The comparison between numerical and experimental pressure-coefficient (C_p) distributions showed generally good agreement in terms of pressure recovery and aerodynamic loading, particularly in the downstream portion of the airfoil where the pressure gradients are less severe. The CFD model successfully reproduced the dominant features of the measured pressure distributions, including the location of the suction peak, the general pressure-recovery behaviour, and the evolution of aerodynamic loading with rear-wing deployment. The largest discrepancies were observed in regions characterized by strong pressure gradients, particularly near the

leading edge of the rear wing. In these areas, the CFD RANS simulations tended to predict stronger suction peaks than those measured experimentally, resulting in a moderate overestimation of aerodynamic loading. This behaviour suggests that the numerical model delays the onset of local separation relative to the experimental flow field, leading to a more attached boundary layer and a smoother pressure recovery, as also reflected in the $\Delta C_{l,veh}$ comparison. This limitation is consistent with the well-known challenges of steady RANS methodologies in accurately predicting localized separation and unsteady flow phenomena in highly loaded aerodynamic configurations. Despite these local discrepancies, the pressure-distribution trends and the integrated aerodynamic coefficients remained in satisfactory agreement with the experimental measurements.

While local discrepancies are observed in regions characterized by strong pressure gradients, the objective of the validation was the assessment of the predictive capability of the numerical model with respect to the integrated aerodynamic quantities governing vehicle performance. For this reason, the comparison of pressure-coefficient distributions is primarily intended to support the interpretation of the underlying flow physics, whereas the quantitative validation is based on the agreement obtained for the global aerodynamic coefficients and their associated experimental uncertainty. The comparison between the Y = 200 mm and Y = 280 mm sections further demonstrates the capability of the numerical model to reproduce not only the pressure levels but also their evolution across the spanwise direction. Despite localized discrepancies near the leading edge, the CFD simulations consistently captured the general shape of the pressure distributions and their variation with rear-wing deployment, supporting the suitability of the adopted methodology for comparative aerodynamic investigations (Figures 9 and 10).

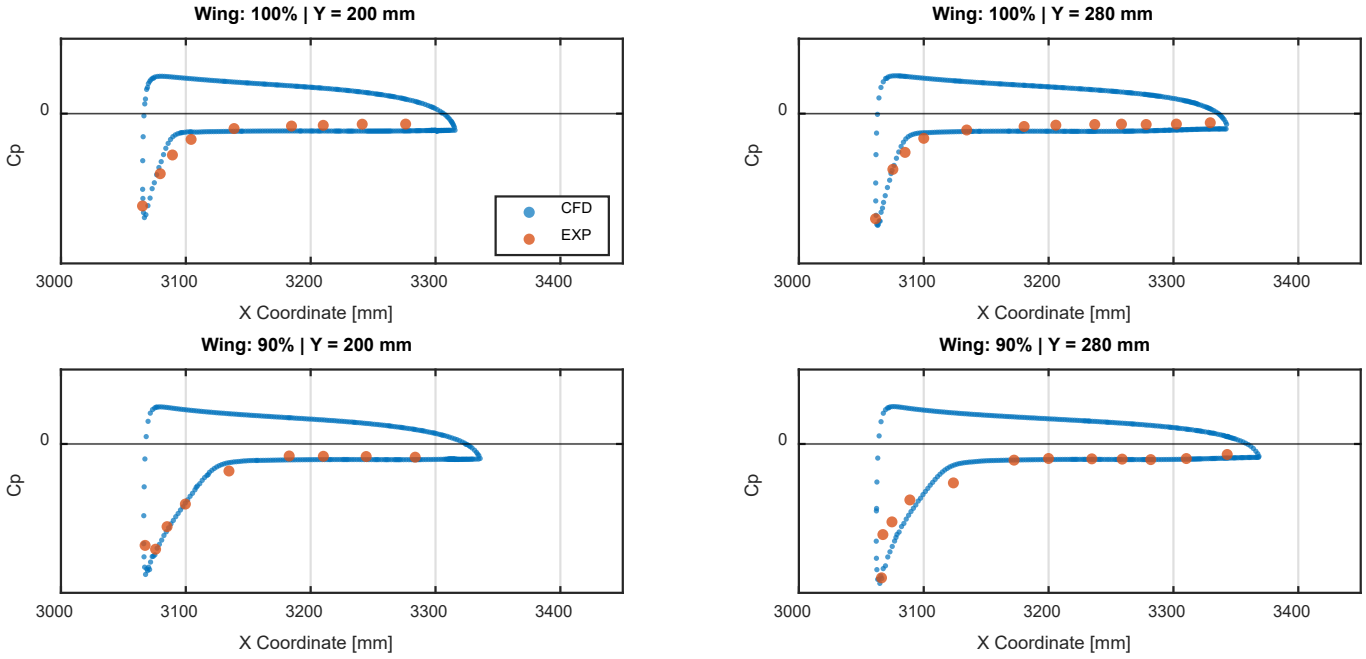


Figure 9. Comparison of pressure-coefficient distributions obtained from CFD and experimental measurements at the v4 operating condition for 90% and 100% rear-wing deployment. The comparison is used to assess the capability of the numerical model to reproduce the measured pressure-loading trends.

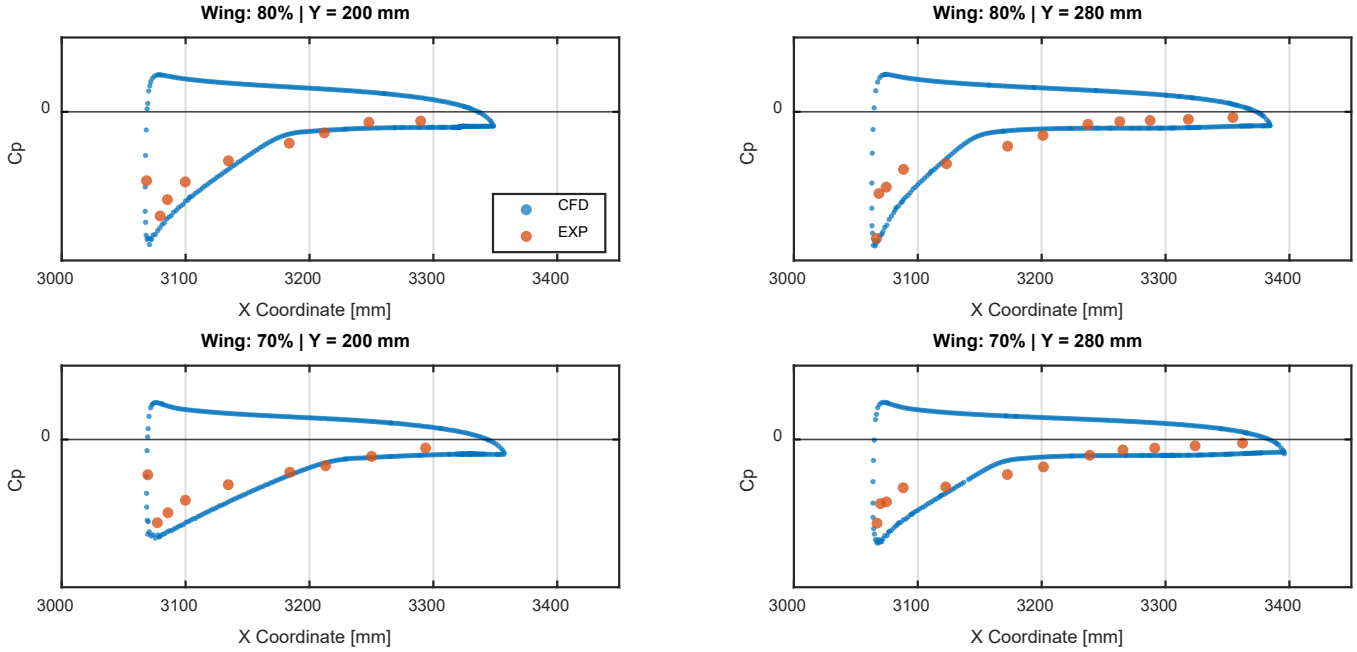


Figure 10. Comparison of CFD-predicted and experimentally measured pressure-coefficient distributions at the v4 operating condition for 70% and 80% rear-wing deployment. The Figure illustrates the pressure-loading distributions used to assess the agreement between numerical and experimental results.

While differences in suction-peak magnitude are observed, the broad distribution shape and pressure-recovery behaviour remain broadly consistent among the analyzed sections. In contrast, rear-wing deployment produces substantially larger variations in the pressure distributions than the spanwise position itself, indicating that deployment angle represents the dominant parameter governing the local aerodynamic loading within the analyzed region. The uncertainty associated with the pressure-coefficient measurements was estimated through uncertainty propagation of the differential-pressure measurements and the Pitot-reference pressure used for normalization. For the investigated operating conditions, the resulting standard uncertainty was of the order of 0.1–0.125 in terms of Cp.

3. Fan Characterization Rig

Once the baseline aerodynamic behaviour of the vehicle had been established through CFD simulations and experimental validation, the next step was to assess the feasibility of the proposed Co-Flow configurations featuring an embedded axial fan within the rear wing. Since the CFD simulations require a realistic representation of fan operating conditions, a dedicated experimental campaign was conducted to determine the pressure–mass flow characteristics of the selected fans under representative operating conditions [37–39].

3.1. Hardware Setup and Test Procedure

A dedicated experimental rig was developed to characterize the aerodynamic and electrical performance of the ducted fans investigated in the present study according to the recommendations of ISO 5801:2017 [37]. The fan was installed at the inlet of a straight circular duct equipped with static pressure taps located immediately upstream and downstream of the rotor, a centreline Pitot probe, and an electronically actuated throttle body used to vary the system resistance and reproduce different operating conditions. The rig enabled the measurement of pressure rise, mass flow rate, electrical power consumption, and fan efficiency over the complete stable operating range for each fan. A schematic representation and a photograph of the experimental setup are reported in Figure 11.

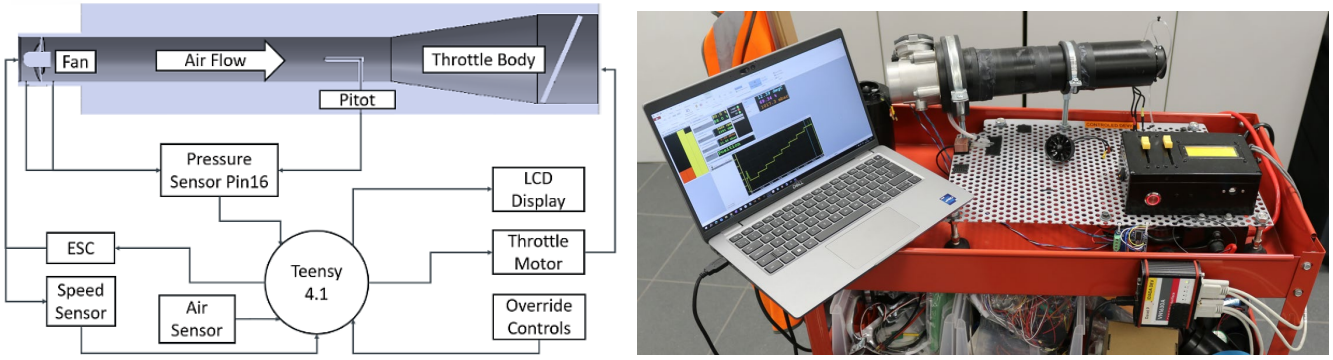


Figure 11. Experimental fan-characterization rig. Schematic representation of the instrumentation and control architecture (**left**) and photograph of the physical test facility (**right**).

Two compact 40-mm ducted axial fans with brushless motor (Table 5) were investigated due to their compatibility with the limited internal volume available within the rear wing.

Table 5. Geometrical and operational characteristics of the investigated 40-mm ducted axial fans.

Model	Ref	De mm	kV	n° Blades	Spacing	Blade Solidity
Galaxy X4 EDF	XF-DFS009	40	5000	12	7.98	0.88
AEORC	XDF40	40	8600	8	12.85	0.757

Static pressure measurements across the fan were acquired using the differential pressure sensor already used for the vehicle baseline experimental campaign; instead, the Pitot delta pressure was acquired with a Texense DPS-190-2.5 differential pressure sensor; moreover, fan rotational speed and electrical power were monitored through the electronic speed controller (ESC) and Isabellenhütte® IVT-S-100A-U0-I-CAN2-12 current sensor.

Due to the relatively low operating Mach number ($M < 0.15$) and the limited pressure rise across the fan, compressibility effects were neglected, and the flow was treated as incompressible. All signals were sampled at 1 kHz and recorded through a CAN-based data acquisition system. Prior to testing, all sensors were calibrated by the instrumentation department using certified calibration procedures, and the resulting calibration curves were implemented within the data acquisition system. Both automated and manual operating modes were employed to identify the stable operating envelope while avoiding surge conditions and excessive vibrations. Unstable operating conditions were observed at throttle openings below 40%; therefore, all automated measurements were performed with a safety margin of 5% above this limit to ensure stable operation and measurement repeatability. The fan performance maps were generated by repeating a sequence of discrete operating conditions at constant rotational speed. For each target RPM, the throttle body was positioned at a predefined opening, and the system was allowed to stabilize for 5 s before a 10 s acquisition interval was recorded. Each operating point was determined from the time-averaged values of pressure rise, mass flow rate, rotational speed, and electrical power. The process was repeated for progressively lower throttle openings until the minimum stable operating condition was reached. To reduce high-frequency fluctuations associated with turbulence, local pressure oscillations, and ESC switching noise, a moving-average filter was applied during post-processing. Atmospheric pressure, temperature, and relative humidity were continuously monitored during testing using a BME280 environmental sensor to account for variations in air density. The density of moist air was calculated as:

$$\rho = \left(\frac{p_d}{R_d T}\right) + \left(\frac{p_v}{R_v T}\right) \tag{3}$$

where p_d is the dry-air partial pressure, p_v the water-vapour partial pressure, R_d and R_v the specific gas constants for dry air and water vapour, respectively, and T the absolute temperature. The airflow velocity was determined from the Pitot pressure measurements according to:

$$V_{center} = \sqrt{\frac{2(P_t - P_s)}{\rho}} \tag{4}$$

where $\boldsymbol{P_t}$ and $\boldsymbol{P_s}$ are the total and static pressures measured by the Pitot tube. Since the probe was located along the duct centerline, the measured velocity was converted into bulk velocity using a correction factor of 0.82 derived from the classical one-seventh power-law turbulent velocity profile:

$$V_{mean} = 0.82\ V_{center} \tag{5}$$

The mass flow rate was then calculated as:

$$\dot{m} = \rho V_{mean} A_p \tag{6}$$

where A_p is the duct cross-sectional area. Fan efficiency was evaluated as the ratio between the aerodynamic power transferred to the airflow and the electrical power absorbed by the electronic speed controller and the motor:

$$\eta = \frac{P_{air}}{P_{mot}} = \frac{q\Delta P}{VA} \tag{7}$$

where q is the volumetric flow rate, ΔP is the pressure rise across the fan, V is the electrical supply voltage, and A is the absorbed current, all acquired instantaneously.

3.2. Repeatability and Uncertainty Assessment

The repeatability of the experimental procedure was assessed through repeated acquisitions performed under identical operating conditions. For each measured quantity, the coefficient of variation (CV%) was calculated as an indicator of signal variability; Table 6 reports the statistics of fan rotational speed, Pitot and static pressure measurements.

Table 6. Repeatability analysis of the fan—rig operating conditions based on the coefficient of variation (CV) of the measured quantities.

Quantity	Mean CV%	Std. Dev of CV%
Fan rotational speed (RPM)	0.64	0.29
Pitot pressure measurements	3.19	0.89
Post-fan static pressure measurements	2.46	0.49

Measurement uncertainty was evaluated according to the GUM methodology by considering the uncertainty contributions associated with the measurement sensors, acquisition system, and environmental conditions.

The resulting standard uncertainties were 0.58 °C for temperature, 0.61 hPa for atmospheric pressure, 1.76%RH for relative humidity, 1.3 mbar for the fan pressure-rise measurement, 0.29 mbar for the Pitot differential pressure measurement, 0.23 A for current, and 0.09 V for voltage. The reported power consumption refers exclusively to the ESC and motor assembly and does not include the power required by the remaining control-system

components. Sensor specifications are reported in Section 2.2, as the same instrumentation was employed for both the vehicle experiments and the fan-characterization campaign.

3.3. Fan Results

Figure 12 reports the measured fan performance maps, showing the relationship between pressure rise and mass flow rate for different rotational speeds. Among the tested solutions, the XFLY fan demonstrated a significantly wider operating range and higher achievable pressure rise compared to the AEORC fan, particularly at elevated mass flow rates. Owing to its wider operating envelope and higher achievable pressure rise, the XFLY fan was selected for the subsequent CFD investigations and experimental assessment of the Co-Flow configurations. During the final stages of the experimental campaign, the AEORC fan experienced blade failure.

The measurements affected by the failure were discarded and are not included in the reported performance maps. Therefore, the event did not influence the results presented in this work, although it prevented further testing. The fan characterization results highlighted the strong sensitivity of the operating point to system resistance.

This behaviour became a key consideration during the Co-Flow design process, since duct geometry, aerodynamic loading, and fan characteristics jointly determined the achievable mass flow rate and jet momentum coefficient under each operating condition.

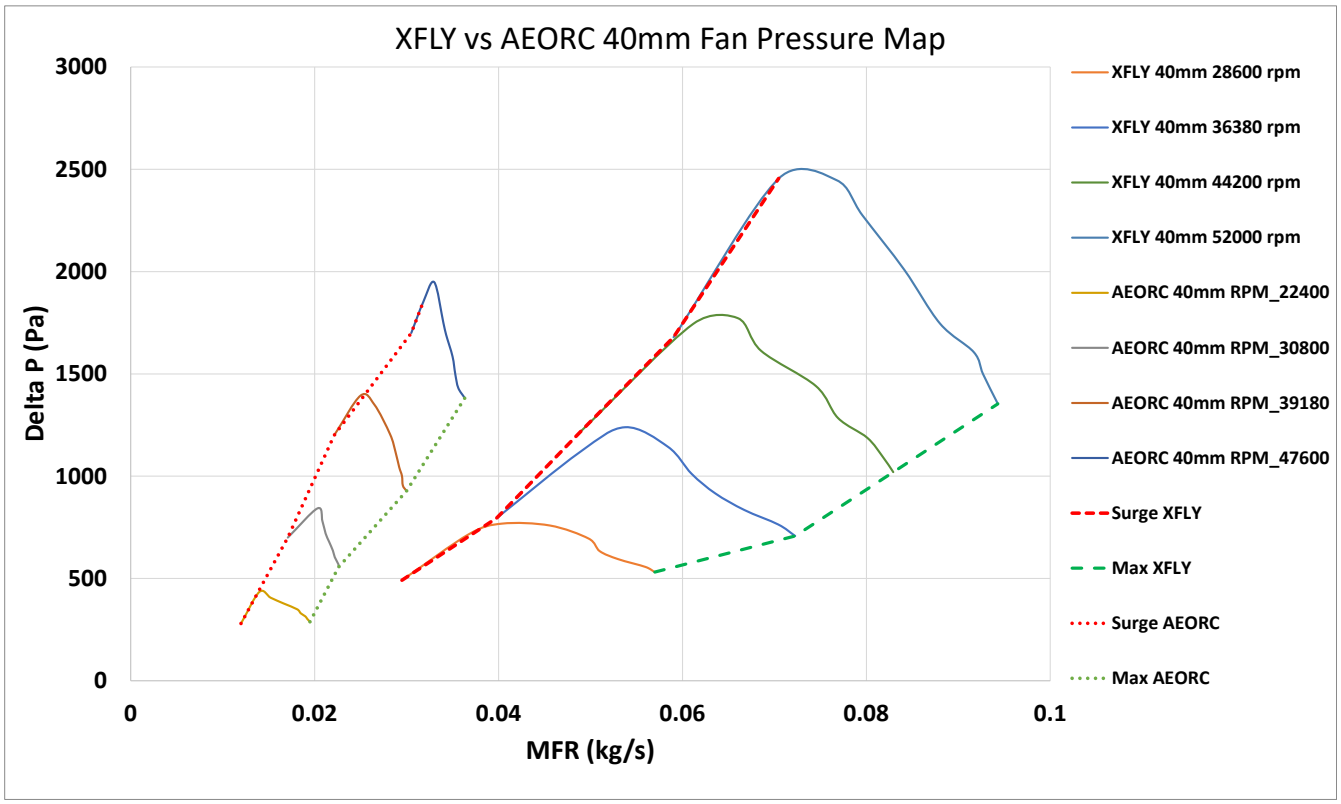


Figure 12. Experimentally measured pressure-rise versus mass-flow-rate characteristics of the investigated ducted fans. The curves were used to determine the operating conditions adopted in the CFD design phase. The operating condition selected for the CFD simulations corresponds to the maximum XFLY fan-speed operating point (52k RPM).

4. Co-Flow System Design and CFD Outcomes

Following the validation of the baseline aerodynamic model, the rear wing was modified to integrate the Co-Flow Jet (CFJ) concept through the implementation of an embedded ducted axial fan. Since the rear-wing assembly and the Co-Flow Jet system

constitute the aerodynamic components directly responsible for the investigated flow-control mechanism, the preliminary design effort focused on the aerodynamic response of this region while retaining the complete vehicle geometry to preserve realistic flow-field interactions and operating conditions. The system was designed to extract air from one region of the wing and re-inject it into another, thereby modifying the local flow field around the rear-wing assembly (Figure 13).

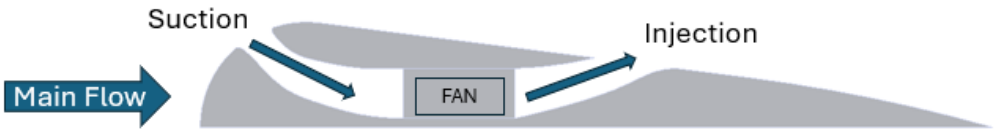


Figure 13. Schematic representation of the front-suction Co-Flow architecture with embedded ducted fan, suction slot, and injection slot.

Unlike most Co-Flow Jet investigations reported in the literature, where the airfoil geometry, slot locations, and internal flow-path architecture are specifically designed and optimized around the active flow-control concept [24–28], the present system was integrated into an existing production-vehicle rear wing originally developed without consideration for Co-Flow actuation, and already passed through various stages of optimization before being used for this research. While recent automotive studies have demonstrated the potential of active flow-control techniques for drag reduction and aerodynamic-performance enhancement, most investigations remain focused on simplified geometries or generic vehicle models rather than production aerodynamic components [8,12,32]. Therefore, the present design was subject to practical constraints associated with the available internal volume, structural layout, packaging of the actuation system, and duct routing, which limited the freedom to optimize slot placement and internal flow paths typically available in purpose-designed CFJ configurations. In particular, the suction and blowing slots could not be positioned excessively close to the leading or trailing edge due to limitations associated with the internal duct layout. In addition, the internal cavity had to accommodate the fans and ducting (Figure 14), electronic speed controller, and pressure instrumentation network. A comprehensive simulation campaign was therefore conducted across a range of wing deployment angles and vehicle speeds; the wing deployment was varied from 70% to 100%, while four representative vehicle speeds (v1–v4, with v1 < v2 < v3 < v4) were considered.

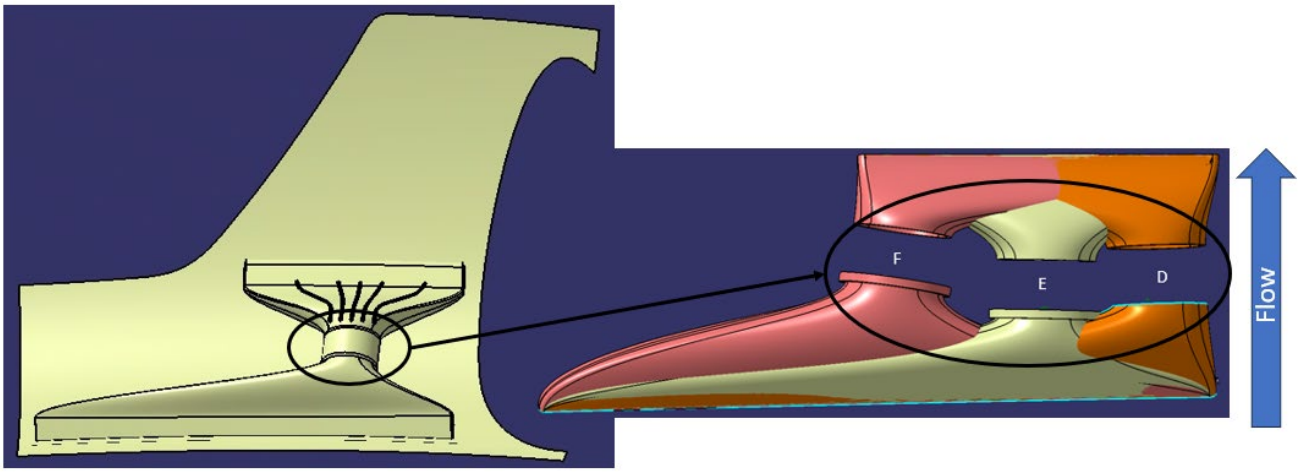


Figure 14. Investigated fan locations within the rear-wing assembly considered during the CFD design campaign.

The CFD simulations were used to support the interpretation of the observed aerodynamic trends and to provide qualitative insight into the associated flow structures. Since no direct flow-field diagnostics such as particle image velocimetry (PIV), wake-rake surveys, or oil-film visualization were performed, the underlying flow mechanisms discussed throughout this section should be regarded as inferred from the combined experimental and numerical evidence rather than directly measured. Although the CFD simulations were conducted on the complete vehicle, the preliminary assessment of the Co-Flow concepts was based on the aerodynamic contribution of the rear-wing assembly only. The CFD-based development process was conducted in two consecutive stages. The first stage focused on the definition of the external Co-Flow architecture, including slot location, slot cross-sectional area, duct inclination, and suction/blowing arrangement. This phase comprised 797 full-vehicle simulations and was used to establish the geometric design guidelines for the Co-Flow system. Representative examples of the investigated geometries are reported in Figure 15. During this stage, the ducted fan was not modelled explicitly. Instead, a uniform velocity boundary condition was imposed within the duct to generate a controlled mass flow rate through the system. The resulting flow was then allowed to develop naturally within the duct and interact with the external aerodynamic field, enabling the aerodynamic effectiveness of different suction and blowing arrangements to be assessed independently from the fan operating characteristics.

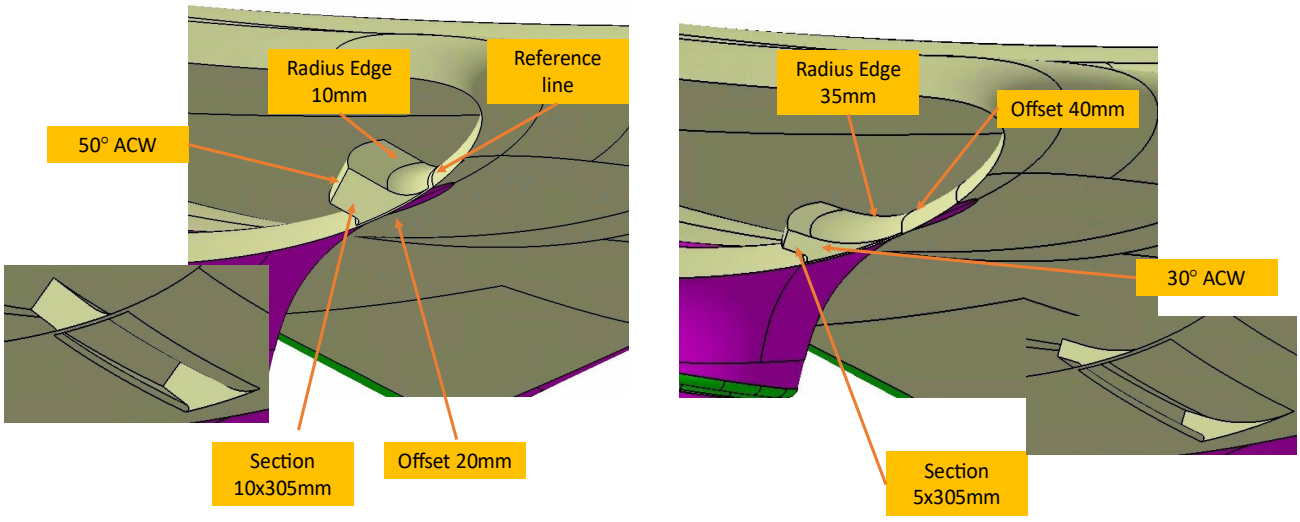


Figure 15. Representative examples of front-suction slot geometries investigated during the parametric CFD study, showing variations in slot position, orientation, radius, and cross-sectional area.

The leading-edge and trailing-edge ducts were initially investigated separately under both suction and blowing conditions. Simulations were performed for imposed flow velocities ranging from 10 to 60 m/s, corresponding to different levels of momentum injection or extraction through the slots. As a result, the total number of simulations was determined not only by the number of investigated geometries but also by the extent of the operating conditions considered. In total, the CFD campaign comprised 885 full-vehicle simulations, 88 baseline cases, and 797 simulations performed using simplified duct configurations. This phase was intended to identify the most promising flow-control architectures and establish the design guidelines for fan-system integration. Each simulation required approximately 5 h of wall-clock time on the available high-performance computing infrastructure. Following the identification of the most promising duct arrangements, the influence of the fan spanwise location within the rear wing was investigated. Three candidate fan positions (D, E, and F) were evaluated using a performance index (PI) based on the aerodynamic response

predicted by CFD. This second design phase comprised an additional 899 full-vehicle simulations and combined the assessment of fan location with the progressive refinement of the internal duct system. The analysis sought not only to identify the most favourable fan location, but also to ensure compatibility between the predicted aerodynamic performance and the achievable operating conditions of the selected fan. All simulations were performed using the experimentally acquired fan map at maximum rotational speed to assess the upper-bound aerodynamic performance under highly loaded operating conditions. This approach allowed the effects of fan location, duct geometry, and operating conditions to be evaluated simultaneously while preserving realistic fan-performance constraints. Because drag reduction and downforce generation represent competing aerodynamic objectives, the PI was formulated as:

$$PI = -\Delta C_{d,wing} + \lambda \Delta C_{l,wing} \tag{8}$$

where λ represents the relative weighting between drag reduction and downforce increase. Three representative values (λ = 0, 0.5 and 1) were considered, corresponding respectively to a drag-driven assessment, an intermediate condition, and an equal weighting of drag and downforce contributions. The performance index is computed exclusively from CFD-predicted aerodynamic coefficients and is used as a screening metric to rank the investigated configurations. Experimental data are not directly included in the PI formulation; however, experimentally measured fan characteristics are incorporated into the CFD simulations to ensure realistic operating conditions.

The performance index (PI) was introduced to rank the investigated Co-Flow configurations during the preliminary CFD screening process. Positive PI values indicate an aerodynamic improvement relative to the baseline configuration, whereas negative values indicate a deterioration. The aerodynamic variations used in the PI formulation are defined as:

$$\Delta C_{d,wing}[\%] = \frac{C_{d,CoFlow} - C_{d,Baseline}}{C_{d,Baseline}} \times 100 \tag{9}$$

$$\Delta C_{l,wing}[\%] = \frac{C_{l,CoFlow} - C_{l,Baseline}}{C_{l,Baseline}} \times 100 \tag{10}$$

The term $\Delta C_{d,wing}$ assigns a positive contribution to drag reduction, while the term $\lambda \Delta C_{l,wing}$ rewards configurations that increase aerodynamic loading. As a result, larger PI values identify more favourable configurations. Throughout this work, the lift coefficient is reported using the automotive sign convention, where positive C_l values represent downforce. Therefore, positive values of $\Delta C_{l,wing}$ correspond to an increase in aerodynamic loading. For each operating condition, all configurations were ranked according to their PI value, and the three best-performing solutions were identified. The occurrence frequency of each configuration within the top-three rankings was then evaluated and averaged across all operating conditions. The resulting occurrence statistics are reported in Figure 16. The ranking statistics indicate that the E-series configurations consistently appear among the highest-performing solutions for all investigated values of λ, demonstrating robustness with respect to the selected weighting factor. Their average occurrence within the top-three rankings is reported in Figure 17. The performance-index analysis consistently identified the E-series configurations as the most effective solutions across the operating conditions investigated. Several configurations were simulated across multiple wing-deployment conditions and vehicle speeds at the maximum mass flow rate permitted by the pressure differential across the Co-Flow ducts. Table 7 summarizes their geometrical details. However, the subsequent analysis of the predicted fan operating points revealed that several of the highest-ranked configurations required operating conditions outside the practical operating envelope of the selected fan. In particular, the available duct sections

generated excessive pressure losses, limiting the achievable mass flow rate and shifting the operating point away from the most efficient region of the fan map.

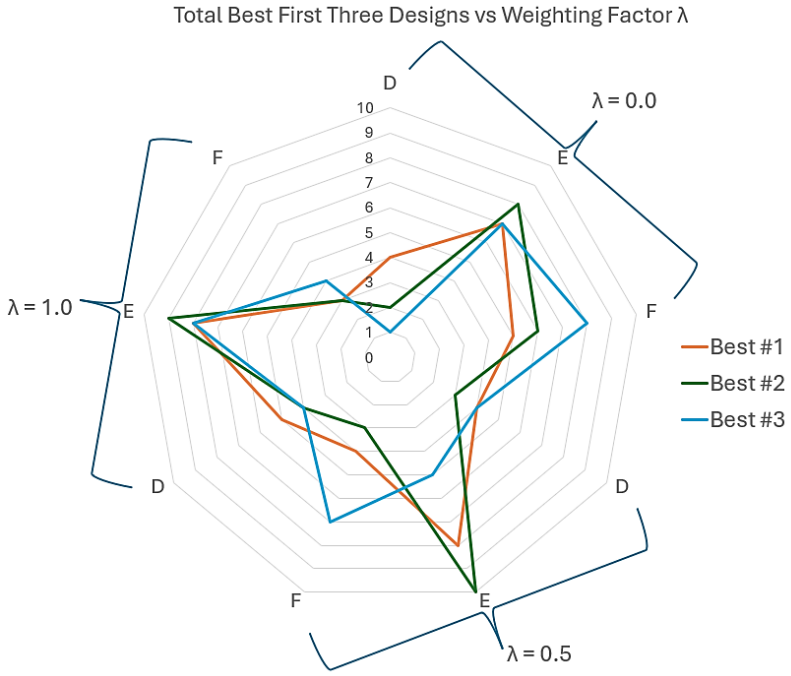


Figure 16. Occurrence frequency of the investigated Co-Flow configurations within the top-three rankings obtained from the performance-index analysis for different values of the weighting factor λ.

Table 7. Geometrical characteristics of the investigated Co-Flow configurations. The dimensions a and b define the front and rear slot cross-sections, from which the corresponding suction and blowing areas can be derived. The listed geometries were assessed during the CFD-based design screening prior to fan-system integration.

	Front Slot Dimensions		Rear Slot Dimensions	
Design	**a mm**	**b mm**	**a mm**	**b mm**
2FS	10	304	5	145
3FS	15	304	5	145
4FS	15	304	7	145
5FS	15	304	12	145
6FS	15	304	17	145
7FB	4.72	304	12	145
8FB	4.72	304	7	145
9aFB	4.72	304	15	145

For this reason, the duct geometries were progressively modified to reduce flow resistance, increase the effective flow area, and improve compatibility with the fan operating characteristics.

This iterative process was conducted within the same CFD campaign and ultimately led to the final E6FS, E8FB, and E9aFB (Figures 18 and 19) configurations selected for manufacturing and experimental validation.

The E6FS configuration employed front suction combined with downstream blowing and represents a particularly demanding operating condition due to the naturally occurring low-pressure region generated by flow acceleration over the wing profile; E8FB and E9aFB adopted the opposite arrangement, with leading-edge blowing and downstream suction,

exploiting the low-pressure region to enhance boundary-layer energization. The E9aFB configuration further introduced an enlarged suction section to increase the achievable mass flow rate and reduce inlet losses even further. The CFD assessment revealed substantial differences among the investigated configurations. Although all designs modified the pressure and velocity fields relative to the baseline case, their aerodynamic response depended strongly on the interaction between the actuation system and the external flow.

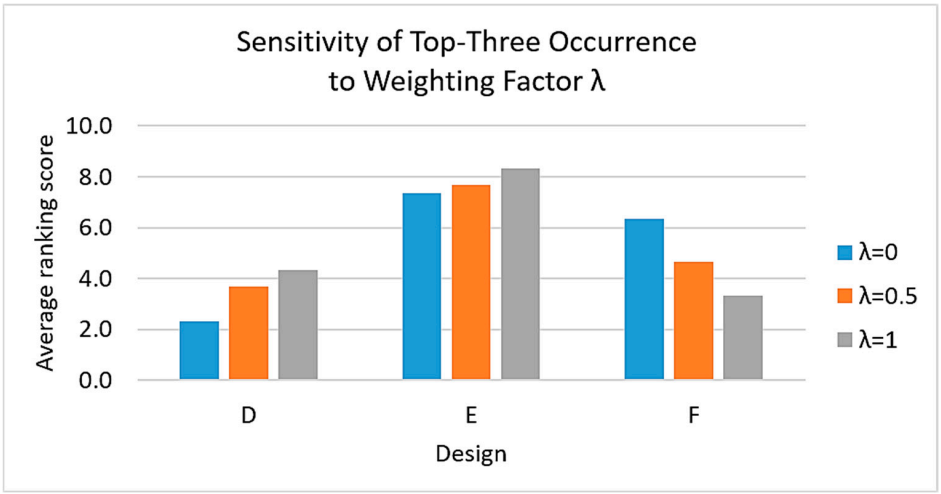


Figure 17. Average occurrence of each configuration within the top-three ranked solutions as a function of the weighting factor λ. For each operating condition, configurations were ranked according to the performance index (PI), and the occurrence frequency within the top three positions was evaluated.

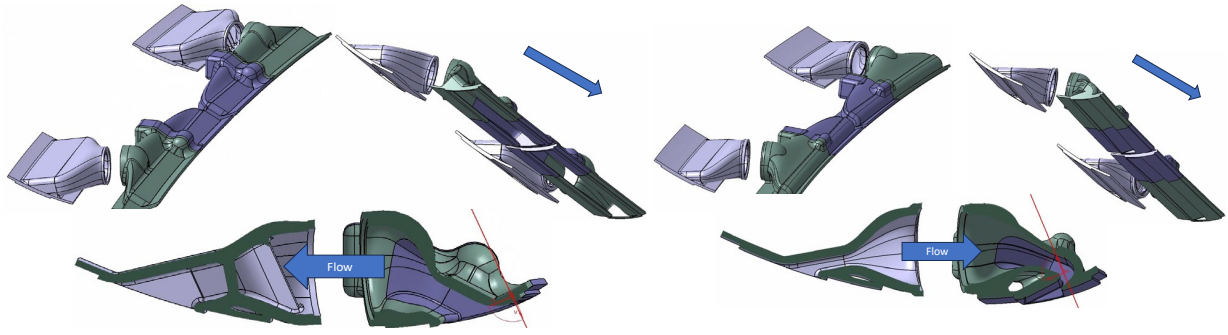


Figure 18. Comparison of the E6FS (**left**) and E8FB (**right**) Co-Flow duct geometries. The E9aFB configuration retains the same front duct layout as E8FB while incorporating an enlarged rear duct inlet section.

Figure 19 compares the pressure and streamline distributions for the baseline configuration and the three Co-Flow architectures at the representative operating condition corresponding to 100% wing deployment and vehicle speed v3. The E6FS configuration produced a pronounced local modification of the flow field around the suction region, indicating a strong interaction between the actuation system and the near-wall flow. However, the corresponding aerodynamic benefit predicted by the CFD analysis remained negligible. For this operating condition, the calculated wing-level aerodynamic variations relative to the baseline configuration were $\Delta C_{l,wing} = -0.1\%$ and $\Delta C_{d,wing} = -0.9\%$. In contrast, both front-blowing configurations generated substantially larger aerodynamic benefits. Under the same operating condition, E8FB achieved $\Delta C_{l,wing} = +7.8\%$ and $\Delta C_{d,wing} = -9.6\%$, while E9aFB produced $\Delta C_{l,wing} = +13.6\%$ and $\Delta C_{d,wing} = -9.0\%$. These results indicate that the magnitude of the local flow perturbation alone is not sufficient to assess the aerodynamic

effectiveness of a Co-Flow configuration. Rather, aerodynamic performance depends on how the injected and extracted momentum modify the global pressure distribution and interact with the aerodynamic loading of the rear wing. Among the investigated solutions, E9aFB provided the largest increase in wing aerodynamic loading, owing to its increased mass-flow capability and enlarged suction section, whereas E8FB achieved comparable drag reductions with a lower actuation demand. The CFD results therefore suggest that Co-Flow effectiveness is governed not only by the amount of injected momentum, but also by the specific architecture through which that momentum is introduced into the flow field. The relative ranking predicted by the CFD analysis is consistent with the trends subsequently observed during the full-scale experimental campaign, supporting the use of the numerical methodology as a comparative design-support tool for Co-Flow configuration development.

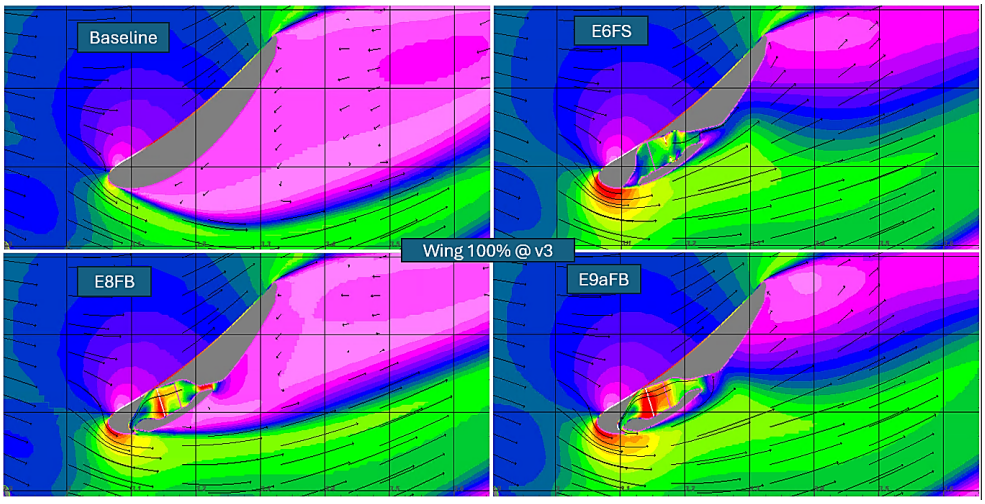


Figure 19. CFD velocity field comparison between the baseline configuration and the E6FS, E8FB, and E9aFB Co-Flow concepts at 100% wing deployment and velocity profile v3, highlighting the flow behaviour in the rear duct inlet region.

The CFD results suggest that Co-Flow effectiveness depends not only on injected momentum, but also on the interaction between the actuation system and the surrounding flow field. Based on the CFD assessment, three Co-Flow configurations (E6FS, E8FB, and E9aFB) were manufactured and integrated into the production-scale rear wing for experimental testing; the internal duct system was fabricated through additive manufacturing (3D printing) to reproduce the complex internal geometries while maintaining acceptable structural stiffness and low mass. The different internal layouts required by the investigated configurations are illustrated in Figure 20, highlighting the integration constraints imposed by the available installation volume within the rear-wing assembly. The aerodynamic performance of the Co-Flow configurations was evaluated using the same metrics adopted for the baseline vehicle. Owing to the active nature of the system, the fan pressure rise, mass flow rate, rotational speed, and electrical power consumption were additionally monitored throughout the experimental campaign. These quantities were used not only to characterize the operating condition of the integrated fan–duct system, but also to assess the aerodynamic benefits achieved by the Co-Flow concept in relation to the corresponding energetic cost. Minor asymmetries between the left and right duct systems generated small differences in operating conditions, which were compensated through a master–slave fan control strategy. Vehicle roll angles were monitored to ensure consistent test conditions, showing a maximum deviation of only 0.1°, well within acceptable limits.

Vehicle testing was intentionally limited to a reduced speed envelope due to structural considerations associated with the modified rear wing assembly. Nevertheless, the selected operating conditions ensured repeatable aerodynamic measurements while preserving structural integrity during testing and operator safety. Figure 21 provides an overview of the final experimental installation on the vehicle. The setup included static-pressure instrumentation integrated within the rear wing, CAN-based data acquisition, fan-speed control hardware, and electrical power monitoring through dedicated voltage and current sensors. This instrumentation enabled the simultaneous measurement of aerodynamic performance, fan operating conditions, and electrical power consumption during the vehicle tests [39]. Following the installation and verification of the complete experimental system, aerodynamic performance measurements were conducted under the operating conditions described previously. To facilitate the interpretation of the aerodynamic response generated by the different Co-Flow configurations, the jet momentum coefficient C_μ was adopted as a non-dimensional measure of the actuation intensity.

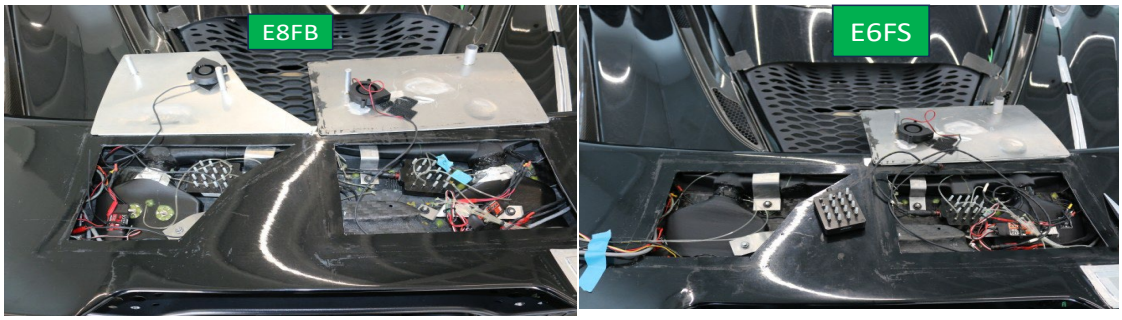


Figure 20. Experimental installation of the Co-Flow system on the test vehicle, showing the E8FB configuration (**left**) and the E6FS configuration (**right**).

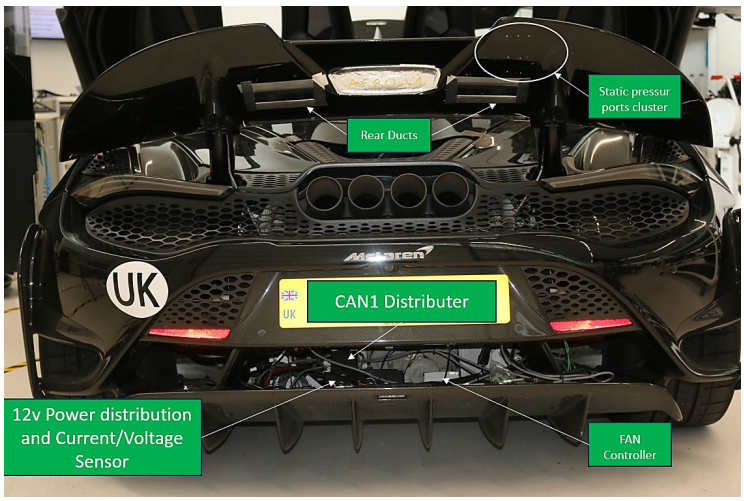


Figure 21. Full-scale vehicle implementation of the Co-Flow Jet system, indicating the rear duct assembly, pressure measurement instrumentation, fan controller, CAN distribution unit, and electrical power monitoring system.

The parameter relates the jet momentum introduced by the Co-Flow system to the freestream dynamic pressure acting on the rear wing and is commonly employed in active-flow-control studies to compare operating conditions characterized by different mass flow rates and vehicle speeds, introduced by Danò [31] as shown in Equation (11):

$$C_\mu = \frac{\dot{m} V_j}{q_\infty A_{ref}} \tag{11}$$

where $\dot{m}$ is the mass flow rate derived from the differential-pressure measurements performed across two duct sections of the Co-Flow ducts, V_j is the slot-exit velocity calculated from the MFR, density and A_j q_∞ is the freestream dynamic pressure, and A_{ref} is the rear-wing reference area. Since the experimental system employed two symmetrically installed fan–duct assemblies, the reported momentum coefficient accounts for the combined contribution of both actuation systems. Unlike conventional CFJ investigations, where the momentum coefficient is typically prescribed through imposed blowing and suction boundary conditions, the values obtained in the present study arise from the coupled interaction between duct geometry, fan operating characteristics, aerodynamic loading, and vehicle operating conditions. Consequently, C_μ should not be interpreted as an independent control parameter, but rather as a resulting system-level quantity reflecting the combined behaviour of the integrated actuation architecture. The jet momentum coefficient was used to characterize actuation intensity and to interpret the aerodynamic response across different vehicle speeds, wing-deployment angles, and Co-Flow configurations.

5. Results and Discussion

This section discusses the aerodynamic behaviour of the investigated Co-Flow configurations through combined CFD and experimental analyses. The results are compared with the baseline configuration in terms of vehicle drag reduction, aerodynamic loading, energetic performance, and local wing pressure distributions, in order to assess the aerodynamic effectiveness and practical feasibility of the proposed active flow-control system. CFD results are used to support the interpretation of the observed aerodynamic trends, while the experimental measurements are used to quantify the resulting aerodynamic and energetic performance.

5.1. Drag Coefficient

This section presents the comparison between the baseline and Co-Flow experimental drag-coefficient ($C_{d,veh}$) results obtained across the investigated rear-wing deployment conditions, including the fully stowed wing configuration. The investigation was conducted to evaluate the influence of the different Co-Flow arrangements on the aerodynamic drag behaviour of the vehicle and to identify the operating conditions under which the active flow-control system provides the largest aerodynamic benefit.

5.1.1. Wing Deployed

The vehicle drag variation relative to the baseline configuration was evaluated experimentally for all investigated Co-Flow systems. The drag variation percentage relative to the baseline was computed using:

$$\Delta C_{d,veh}[\%] = \frac{C_{d,CoFlow} - C_{d,Baseline}}{C_{d,Baseline}} \times 100 \quad (12)$$

where $C_{d,CoFlow}$ is the drag coefficient with the Co-Flow system installed and $C_{d,Baseline}$ corresponds to the unmodified wing. Negative values of $\Delta C_{d,veh}$ indicate drag reduction relative to the baseline configuration, whereas positive values indicate a drag penalty. The three investigated configurations exhibit markedly different drag responses across the tested operating envelope (Figure 22). At low wing deployment (70–80%), the observed changes remain relatively modest for all configurations. Under these conditions, the E6FS configuration generally produces a drag penalty, while E8FB and E9aFB provide limited but measurable drag reductions. At higher wing deployment levels (90–100%), larger drag reductions are observed, particularly for the front-blowing configurations E8FB and E9aFB. Among the investigated solutions, E9aFB achieves the largest drag reduction, reaching

approximately 9% under the most favourable operating conditions. E8FB also produces consistent drag reductions across a broad range of operating conditions. In contrast, E6FS does not consistently outperform the baseline configuration and remains characterized by less favourable drag performance throughout much of the investigated operating envelope.

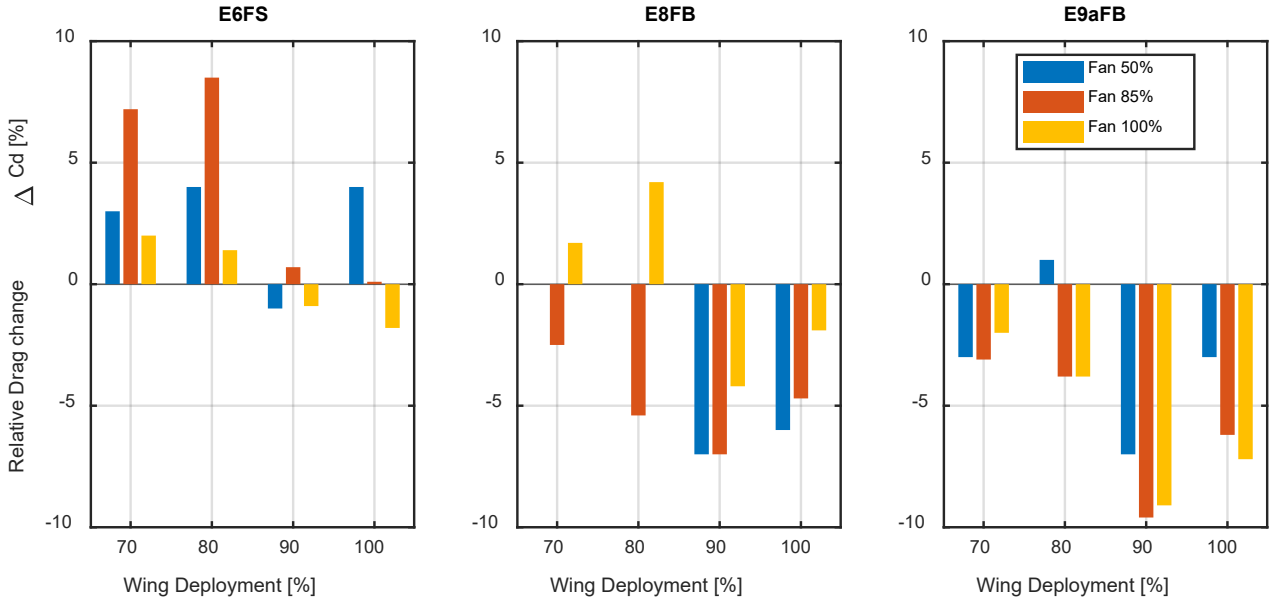


Figure 22. Vehicle experimental variation in drag coefficient relative to the baseline configuration for E6FS, E8FB, and E9aFB designs across different wing deployment positions and fan operating conditions.

The influence of fan speed is not uniform across all operating conditions. Increasing fan speed does not always result in larger drag reductions, and the maximum fan speed does not systematically correspond to the largest aerodynamic benefit. This behaviour is observed for both E8FB and E9aFB, particularly at intermediate wing-deployment conditions. It should be noted that, during the coastdown tests used for drag evaluation, the momentum coefficient C_μ was not a fixed parameter but varied continuously with vehicle speed and fan operating condition throughout the deceleration process. Therefore, unlike the downforce measurements conducted under steady-state conditions, no unique C_μ value can be associated with a given drag test. For this reason, a detailed analysis of C_μ is presented in the lift assessment, where steady operating conditions allow a more rigorous interpretation of the actuation intensity. Nevertheless, the drag results clearly show that the front-blowing configurations (E8FB and E9aFB) provide the most effective drag-reduction performance within the investigated operating range, while E6FS delivers comparatively limited aerodynamic benefits.

5.1.2. Wing Fully Stowed

Additional measurements were performed with the rear wing fully stowed to evaluate the aerodynamic impact of the duct openings required by the Co-Flow system and to assess the system behaviour under conditions of minimal rear-wing loading (Figure 23). Based on the results obtained for the deployed-wing configurations, E6FS exhibited limited aerodynamic benefits throughout the investigated operating range and was therefore not considered for further testing under fully stowed conditions. Consequently, the analysis was restricted to the E8FB and E9aFB configurations. To maintain consistency with the practical-feasibility objectives of the study, the investigation was limited to fan operating conditions up to 50% speed. While higher fan speeds were technically achievable, continuous operation under such conditions would inevitably increase energy consumption,

acoustic emissions, and mechanical loading of the actuation system. Therefore, only the 0%, 30%, and 50% fan-speed operating points were considered for the fully stowed wing configuration. Under these conditions, the aerodynamic response differs substantially from that observed for the deployed-wing cases. The E8FB configuration consistently produces a drag penalty across the investigated fan-speed range, with drag increases between approximately 3% and 5% relative to the baseline configuration. In contrast, E9aFB exhibits a progressive improvement as fan speed increases. While a drag penalty is observed at low actuation levels, the aerodynamic response improves with increasing fan speed and transitions to a net drag reduction at 50% fan speed, reaching approximately 4% under the investigated conditions. Compared with the deployed-wing cases, the magnitude of the aerodynamic benefit is generally reduced when the wing is fully stowed. Nevertheless, the outcomes indicate that measurable drag reductions can still be achieved for selected configurations and operating conditions. Among the investigated solutions, E9aFB remains the most effective configuration, whereas E8FB does not provide a drag benefit within the tested operating range.

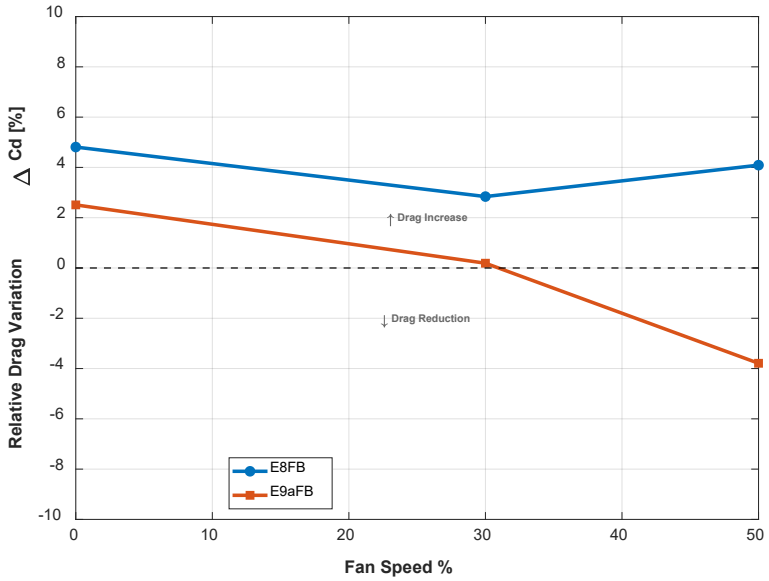


Figure 23. Vehicle experimental drag coefficient variation at 0% wing deployment as a function of fan speed for the E8FB and E9aFB configurations relative to the baseline case.

5.2. Lift Coefficient

The variation in lift coefficient relative to the baseline configuration was evaluated to determine the impact of the Co-Flow system on aerodynamic loading and computed as:

$$\Delta C_{l,veh}[\%] = \frac{C_{l,CoFlow} - C_{l,Baseline}}{C_{l,Baseline}} \times 100 \quad (13)$$

where $C_{l,CoFlow}$ is the lift coefficient with the Co-Flow system active and $C_{l,Baseline}$ corresponds to the baseline configuration. Positive values of $\Delta C_{l,veh}$ indicate an increase in downforce relative to the baseline case, whereas negative values indicate a reduction.

The operating points v1 to v4 correspond to increasing vehicle speed. The lift variation obtained for the three investigated Co-Flow configurations is discussed together with the corresponding jet momentum-coefficient distributions.

This combined analysis provides insight into the relationship between aerodynamic performance and actuation intensity across the investigated range of wing deployments, vehicle speeds, and fan operating conditions. The E6FS configuration exhibits a reduction in aerodynamic loading across the entire investigated operating range (Figure 24).

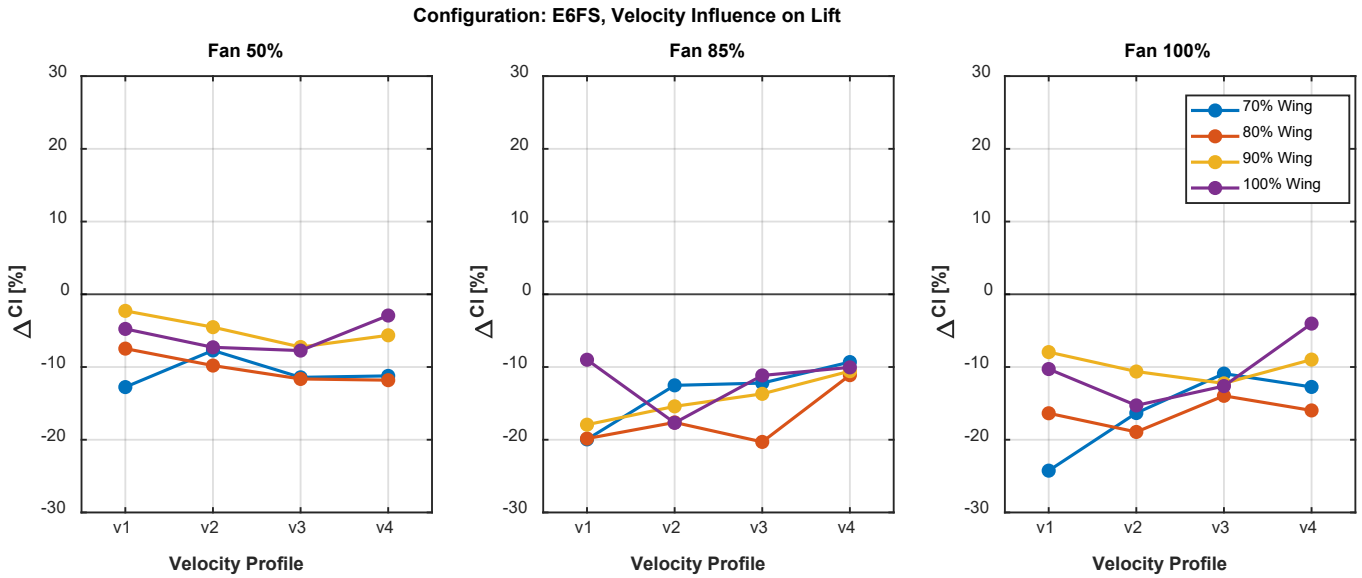


Figure 24. Influence of vehicle velocity profile and wing deployment position on the experimental vehicle lift coefficient variation in the E6FS configuration relative to the baseline case for different fan operating speeds.

Negative values of $\Delta C_{l,veh}$ are observed for all tested fan speeds, wing deployments, and vehicle-speed conditions, indicating that the Co-Flow system does not provide a measurable downforce benefit for this configuration. Depending on the operating condition, downforce penalties typically range between approximately 5% and 25% relative to the baseline vehicle. To support the interpretation of these results, the corresponding jet momentum-coefficient distributions are reported in Figure 25. As expected, C_μ increases with fan speed and decreases with vehicle speed. The highest momentum-coefficient values are consistently observed at 100% wing deployment, whereas the lowest values occur at 70% deployment, reflecting the strong interaction between wing operating condition and the operating point of the integrated fan-duct system. Despite spanning more than one order of magnitude across the investigated operating envelope, the momentum coefficient does not produce corresponding improvements in aerodynamic loading. The measured values of $\Delta C_{l,veh}$ remain consistently negative, and no clear relationship between increasing C_μ and improved aerodynamic performance can be identified. In several cases, the largest aerodynamic penalties are associated with the highest momentum-coefficient conditions, particularly at low vehicle speeds.

The results indicate that increasing the available actuation intensity alone is insufficient to generate a beneficial aerodynamic response for the front-suction architecture. This observation suggests that the effectiveness of the Co-Flow system depends not only on the magnitude of the injected momentum but also on how that momentum is introduced into the flow field through the duct arrangement. A markedly different behaviour is observed for the E8FB configuration (Figure 26). Compared with E6FS, E8FB produces measurable increases in downforce over a substantial portion of the investigated operating range. Positive values of $\Delta C_{l,veh}$ are obtained for several combinations of wing deployment, vehicle speed, and fan operating condition, with the largest improvements generally observed at 100% fan speed. Depending on the operating condition, $\Delta C_{l,veh}$ varies from approximately -10% to $+15\%$.

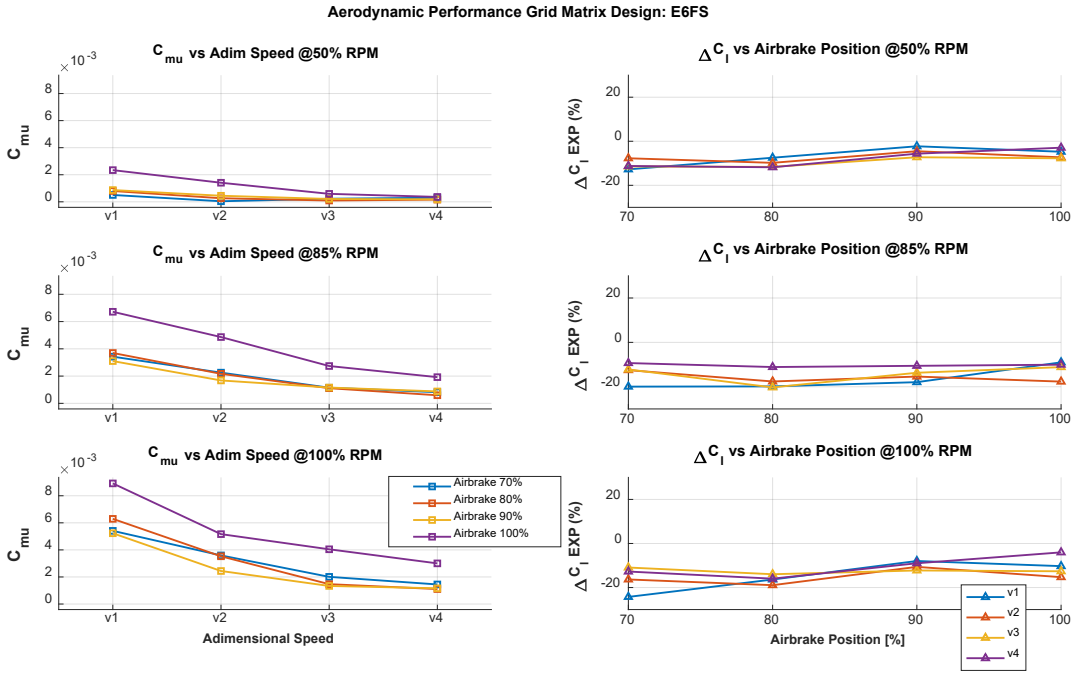


Figure 25. Vehicle experimental aerodynamic performance matrix for the E6FS configuration, showing momentum coefficient variation with dimensionless velocity and vehicle lift coefficient variation with airbrake position at different fan speeds.

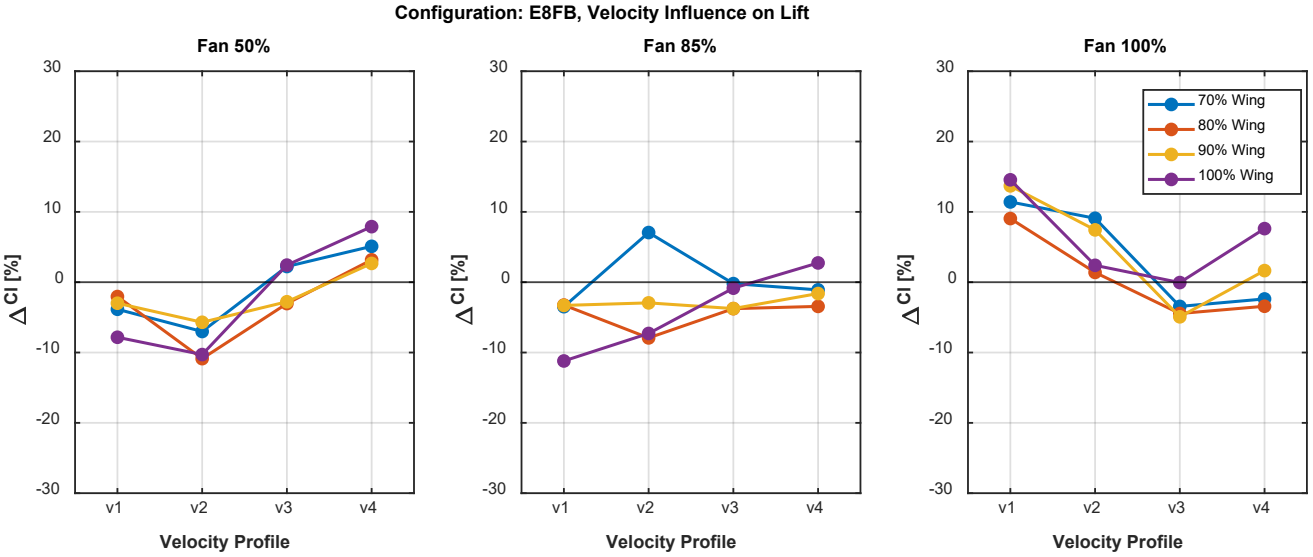


Figure 26. Influence of vehicle velocity profile and wing deployment position on the experimental vehicle lift coefficient variation in the E8FB configuration relative to the baseline case for different fan operating speeds.

To support the interpretation of these results, the corresponding jet momentum-coefficient distributions are reported in Figure 27. Similar to E6FS, the jet momentum coefficient increases with fan speed and decreases with vehicle speed. However, E8FB generally operates at lower C_μ levels than E6FS due to the reduced mass flow rate delivered by the integrated fan-duct system. Despite operating at lower momentum-coefficient levels than E6FS, E8FB provides substantially improved aerodynamic performance, highlighting the importance of duct architecture in determining Co-Flow effectiveness. Unlike E6FS, E8FB exhibits a progressive improvement in aerodynamic loading as the actuation level

increases. At low fan-speed settings, the response remains mixed, whereas positive values of $\Delta C_{l,veh}$ become increasingly common as fan speed increases. As fan speed increases, positive values of $\Delta C_{l,veh}$ become increasingly common and larger improvements in downforce are achieved. This trend suggests that the available momentum injection becomes sufficiently effective only above a certain actuation level. Nevertheless, the relationship between $\Delta C_{l,veh}$ and C_μ is not monotonic. For all investigated fan-speed settings, a distinct deterioration in aerodynamic performance is observed around the v3 operating condition, followed by a recovery at v4, despite the comparatively smooth variation of C_μ with vehicle speed. The persistence of this local minimum suggests that the aerodynamic response cannot be explained solely by the magnitude of the injected momentum. While increasing C_μ generally improves the performance of E8FB, additional factors associated with the aerodynamic operating condition clearly influence the resulting aerodynamic benefit. The specific flow mechanisms responsible for this behaviour cannot be identified from the present dataset and would require dedicated flow-field measurements for further investigation. The analysis suggests that the E8FB configuration provides substantially better aerodynamic performance than E6FS and demonstrates the capability of generating measurable increases in vehicle downforce over a broad range of operating conditions. To further increase the available actuation intensity, the E9aFB configuration was developed by enlarging the inlet section identified as a flow restriction in the previous E8FB design. The corresponding jet momentum-coefficient distributions are reported in Figure 28.

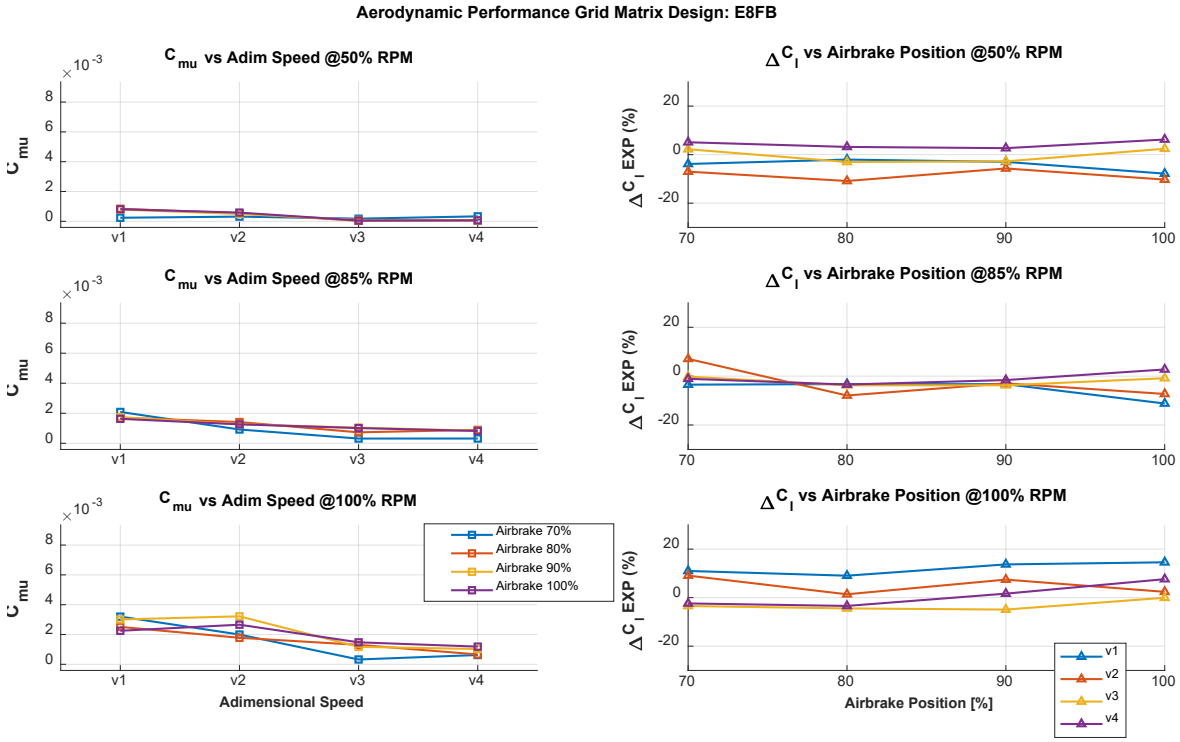


Figure 27. Vehicle experimental aerodynamic performance matrix for the E8FB configuration, showing momentum coefficient variation with dimensionless velocity and vehicle lift coefficient variation with airbrake position at different fan speeds.

Compared with E8FB, E9aFB consistently operates at higher C_μ levels across the investigated operating range. This behaviour reflects the increase in measured mass flow rate resulting from the enlarged inlet geometry and is consistent with the CFD predictions, which indicated reduced flow restriction for this configuration. The aerodynamic response of E9aFB differs from that observed for E8FB. Whereas E8FB generally requires higher

actuation levels to achieve consistent downforce benefits, E9aFB produces positive values of $\Delta C_{l,veh}$ over a larger portion of the investigated operating envelope, including several low-actuation conditions (Figure 29). At both 50% and 85% fan speed, positive downforce variations are already observed at the lower vehicle-speed conditions, indicating that the additional mass-flow capability improves the effectiveness of the Co-Flow system.

However, the increase in momentum coefficient does not translate into proportional aerodynamic gains. Although E9aFB operates at substantially higher C_μ levels than E8FB, the aerodynamic improvements remain of similar magnitude and the characteristic deterioration in performance observed around the v3 operating condition persists across all investigated fan-speed settings. This behaviour suggests that increasing the available momentum alone is insufficient to guarantee proportional improvements in aerodynamic loading. Furthermore, the persistence of the local minimum around v3, despite the substantial increase in C_μ relative to E8FB, indicates that the fluid-dynamic response is governed by the combined interaction between momentum injection, external aerodynamic loading, and operating condition rather than by a single critical momentum-coefficient threshold.

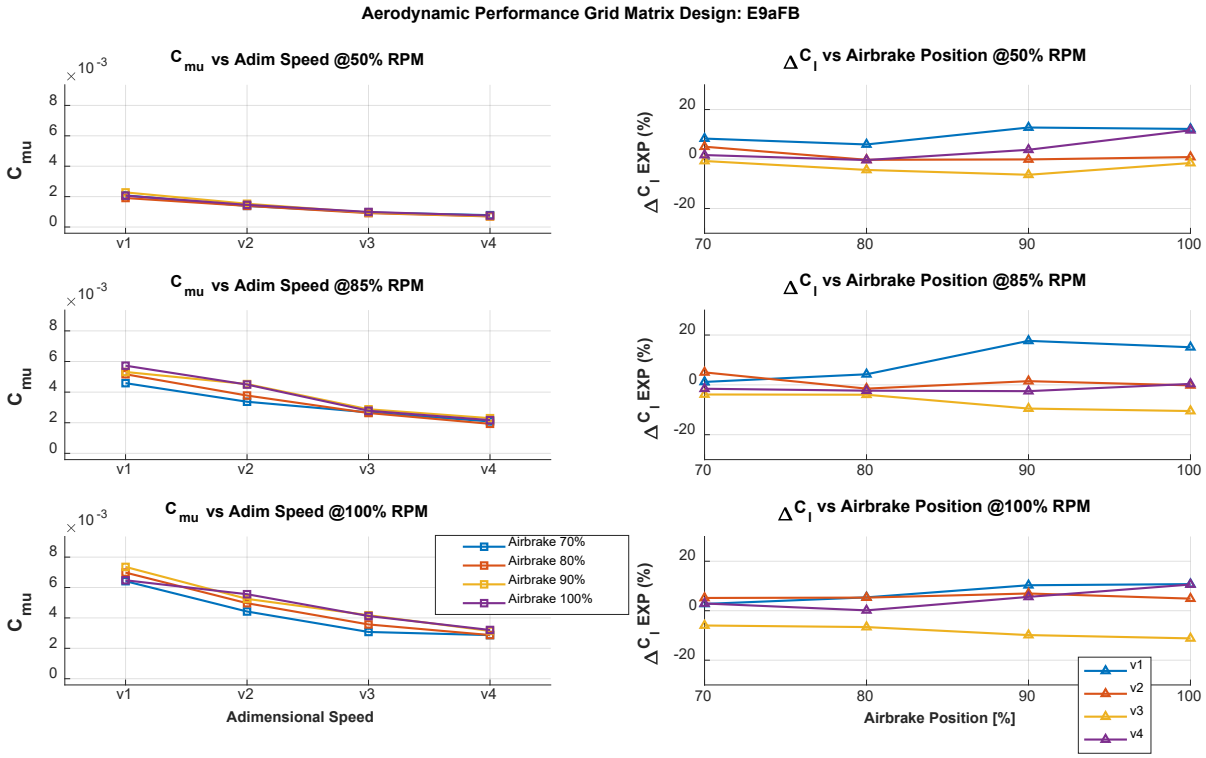


Figure 28. Vehicle experimental aerodynamic performance matrix for the E9aFB configuration, showing momentum coefficient variation with dimensionless velocity and vehicle lift coefficient variation with airbrake position at different fan speeds.

While C_μ remains a useful parameter for characterizing actuation intensity, no unique momentum-coefficient value associated with the observed deterioration in aerodynamic performance could be identified from the present dataset.

The E9aFB results indicate that the enlarged inlet geometry successfully increases the available actuation authority and broadens the range of operating conditions for which positive aerodynamic benefits can be obtained. The additional momentum is not converted into proportional increases in downforce, highlighting the complex relationship between momentum injection and aerodynamic effectiveness in integrated Co-Flow systems. A further insight emerges from the comparison between the E8FB configuration operating at 100% fan speed and the E9aFB configuration operating at 50% fan speed (Figure 30).

Although the two configurations employ different duct geometries and operate at substantially different fan speeds, they produce aerodynamic responses that are remarkably similar across the investigated vehicle-speed range. In both cases, positive values of $\Delta C_{l,veh}$ are obtained at the lower vehicle-speed conditions, followed by a pronounced deterioration around the v3 operating condition and a subsequent recovery at v4. The similarity of the resulting aerodynamic trends is particularly noteworthy because the comparable performance is achieved using significantly different actuation strategies. This observation further indicates that fan rotational speed alone is not an adequate parameter for characterizing the aerodynamic response of the Co-Flow system. The comparison also highlights that increasing the available actuation intensity does not necessarily translate into proportional aerodynamic gains. Despite the substantially higher fan speed required by E8FB, its aerodynamic response remains comparable to that obtained by E9aFB operating at only 50% fan speed. This behaviour suggests that the improved duct architecture of E9aFB enables a more effective utilization of the available actuation authority. More importantly, the persistence of the local minimum around the v3 operating condition in both configurations indicates that the flow response cannot be described solely by either fan speed or jet momentum coefficient, as explained before. While C_μ remains a useful parameter for characterizing actuation intensity, the recurring deterioration observed at v3 across different configurations and operating conditions suggests that additional factors associated with the aerodynamic operating condition continue to play an important role in determining the effectiveness of the Co-Flow system.

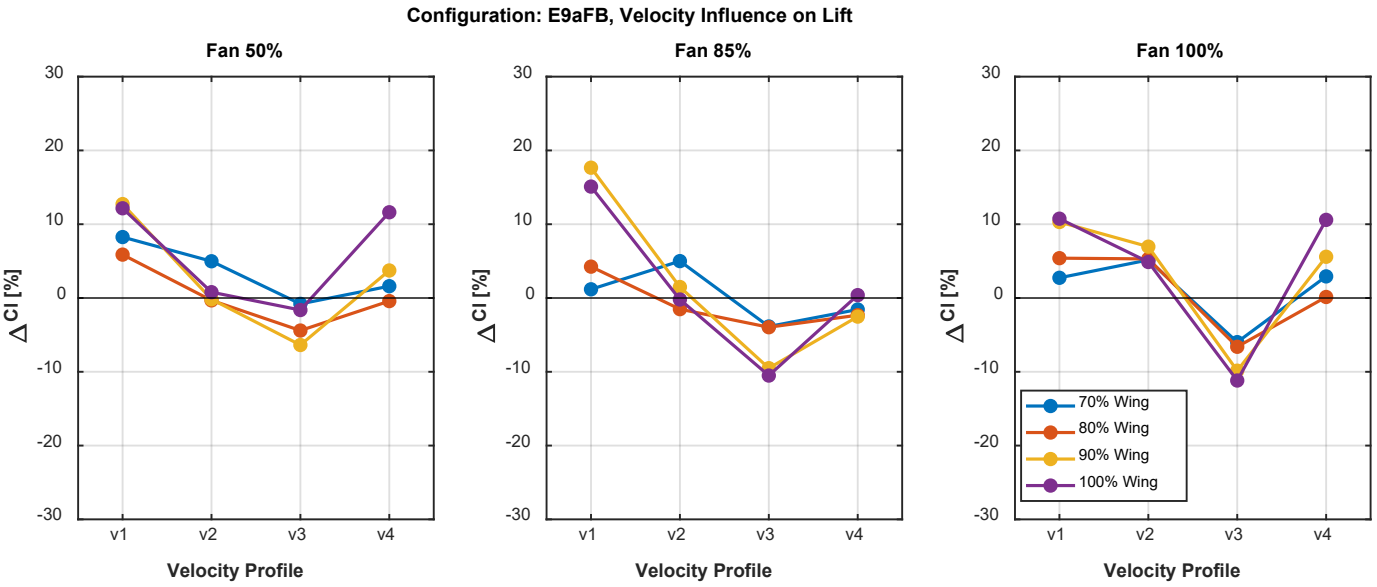


Figure 29. Influence of vehicle velocity profile and wing deployment position on the experimental vehicle lift coefficient variation in the E9aFB configuration relative to the baseline case for different fan operating speeds.

Results show that the lift measurements demonstrated a clear progression in aerodynamic performance across the investigated Co-Flow configurations. The E6FS arrangement does not provide measurable downforce benefits despite operating at relatively high momentum-coefficient levels. In contrast, both front-blowing configurations generate significant increases in aerodynamic loading over a substantial portion of the investigated operating range. The comparison between E8FB and E9aFB further indicates that improvements in aerodynamic performance are linked not only to the magnitude of the injected momentum but also to the effectiveness with which that momentum is introduced into the flow field through the duct architecture.

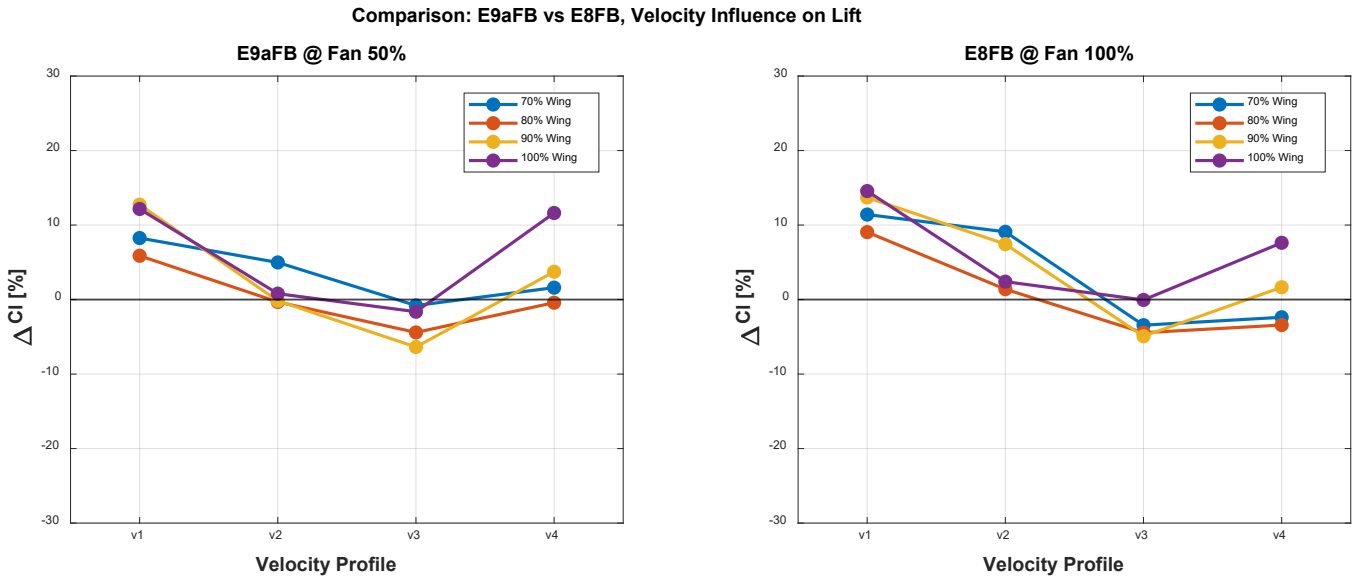


Figure 30. Comparison of the vehicle lift coefficient variation obtained with the E9aFB configuration at 50% fan speed and the E8FB configuration at 100% fan speed for different wing deployment positions and velocity profiles.

5.3. Pressure Coefficient

The pressure-coefficient distributions were first analyzed through CFD simulations on the wing section aligned with the fan centerline. This comparison enables the flow behaviour of the different Co-Flow configurations to be evaluated under identical operating conditions, including the E9aFB configuration for which complete experimental data were not available. Compared with the baseline configuration, all Co-Flow designs produce noticeable modifications of the pressure distribution within the leading-edge region and over the portion of the wing directly influenced by the actuation system (Figure 31). Among the investigated solutions, E9aFB produces the most pronounced modification of the pressure distribution within the controlled region, whereas E6FS exhibits a less uniform pressure recovery. In contrast, both E8FB and E9aFB generate smoother pressure-distribution trends over the instrumented section. The influence of the Co-Flow system progressively decreases away from the fan centerline, where three-dimensional flow effects and support-induced flow structures become increasingly important. However, the CFD comparison reveals clear differences between the investigated configurations, highlighting the sensitivity of the pressure-field response to the selected blowing-suction arrangement and to the interaction between the injected flow and the external aerodynamic field.

The CFD predictions were subsequently compared against experimental pressure measurements obtained from the instrumented wing section aligned with the fan centerline.

Good agreement was observed between numerical and experimental C_p distributions, indicating that the CFD model correctly captures the global pressure trends and the relative aerodynamic behaviour of the investigated configurations (Figures 32 and 33). The largest discrepancies occur near the leading edge and in regions characterized by strong adverse pressure gradients, where the steady RANS simulations tend to predict a more attached flow than that observed experimentally. This behaviour is particularly evident for the E6FS configuration, whose experimental C_p distributions exhibit localized deviations from the numerical predictions. Conversely, E8FB exhibits a smoother pressure recovery and a closer agreement between CFD and experimental pressure distributions, indicating that the aerodynamic response is captured more consistently by the numerical model than in the E6FS configuration.

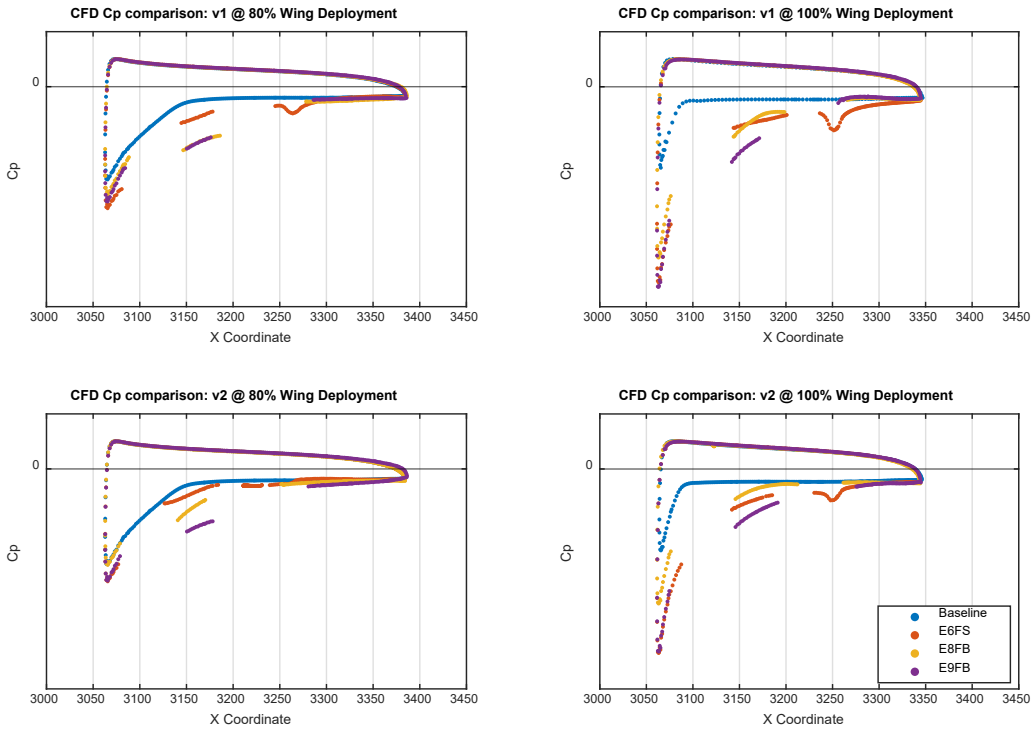


Figure 31. Comparison of CFD-predicted local pressure coefficient distributions on the rear wing section (Section 280 mm) for the baseline, E6FS, E8FB, and E9aFB configurations at velocity profiles v1 and v2, 80% and 100% wing deployment, and 100% fan speed.

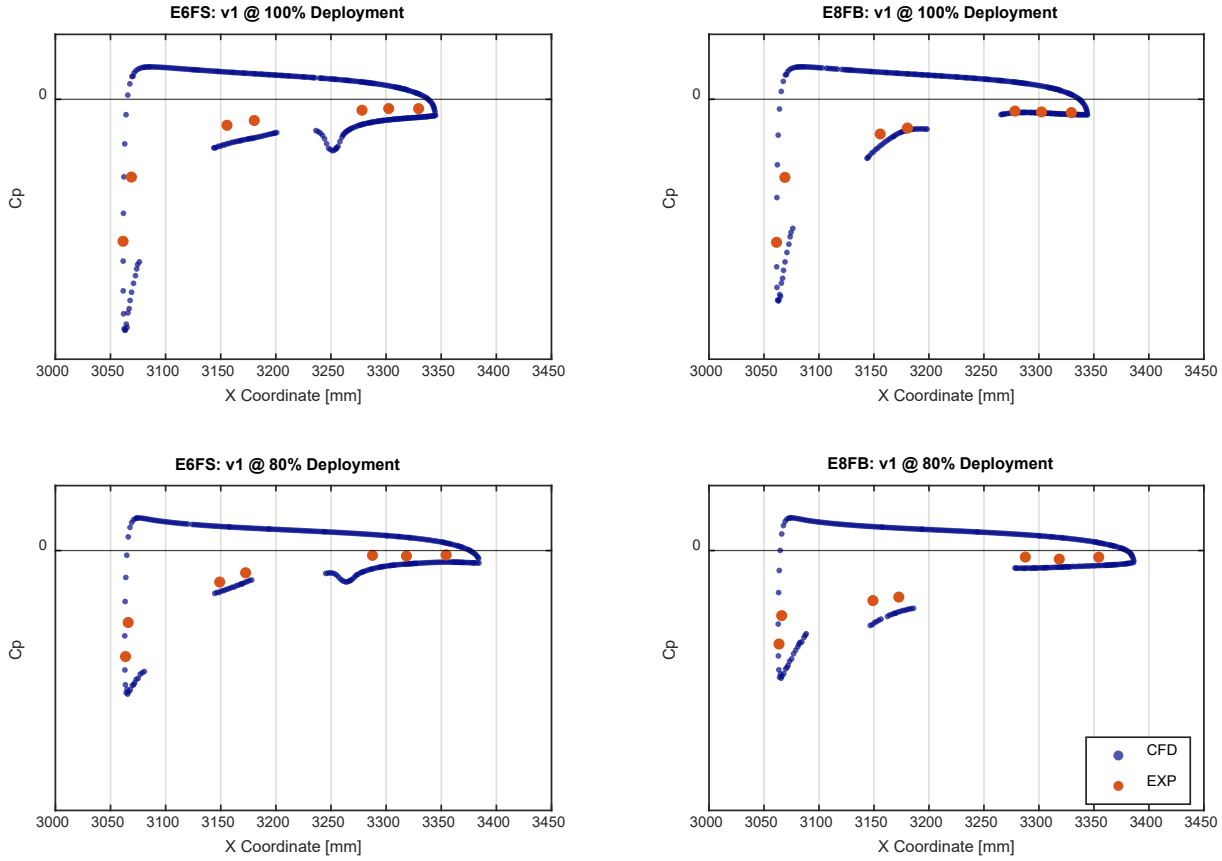


Figure 32. Comparison between CFD predictions and experimentally measured local pressure coefficient distributions on the rear wing section (Section 280 mm) for the E6FS and E8FB configurations at velocity profile v1, 80% and 100% wing deployment, with the Co-Flow system operating at 100% fan speed.

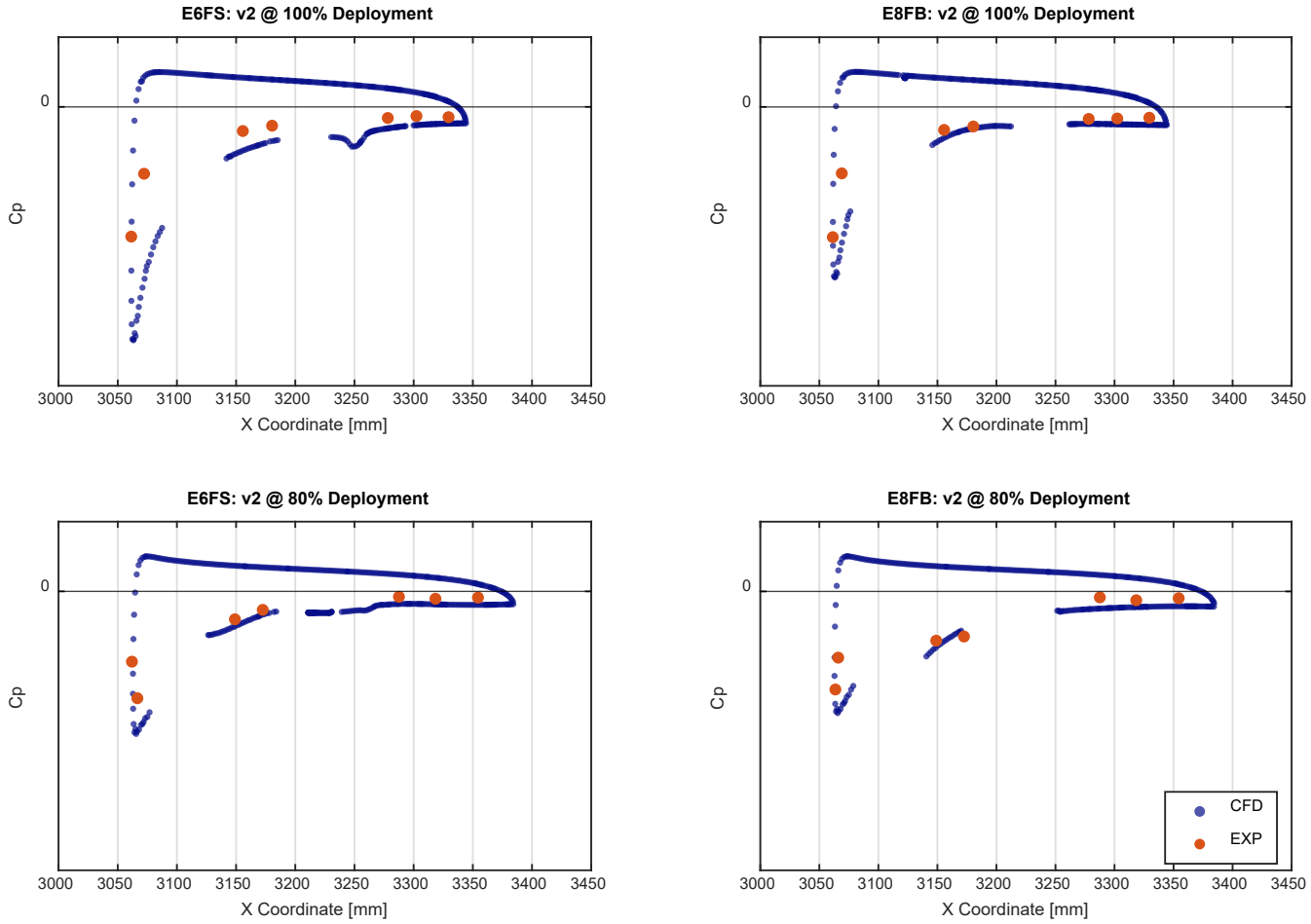


Figure 33. Comparison between CFD predictions and experimentally measured local pressure coefficient distributions on the rear wing section (Section 280 mm) for the E6FS and E8FB configurations at velocity profile v2, 80% and 100% wing deployment, with the Co-Flow system operating at 100% fan speed.

Experimental comparisons against the baseline configuration further confirm that the Co-Flow system modifies the pressure distribution over the rear-wing surface.

Both E6FS and E8FB generate increased suction levels near the leading-edge region relative to the baseline configuration, with E8FB generally producing the largest deviations from the baseline pressure distributions (Figures 34 and 35).

The observed pressure-distribution differences become progressively more pronounced as wing deployment increases, whereas smaller deviations are generally observed under lower aerodynamic-loading conditions.

This behaviour indicates that the influence of the Co-Flow system becomes more evident under highly loaded wing conditions. The largest pressure-distribution modifications are generally observed at high wing-deployment settings and low vehicle speeds, which also correspond to the operating conditions associated with the highest momentum-coefficient levels.

As vehicle speed increases, the available momentum coefficient decreases due to the increase in freestream dynamic pressure, and the relative influence of the Co-Flow system on the pressure distributions generally becomes smaller (Figures 36 and 37).

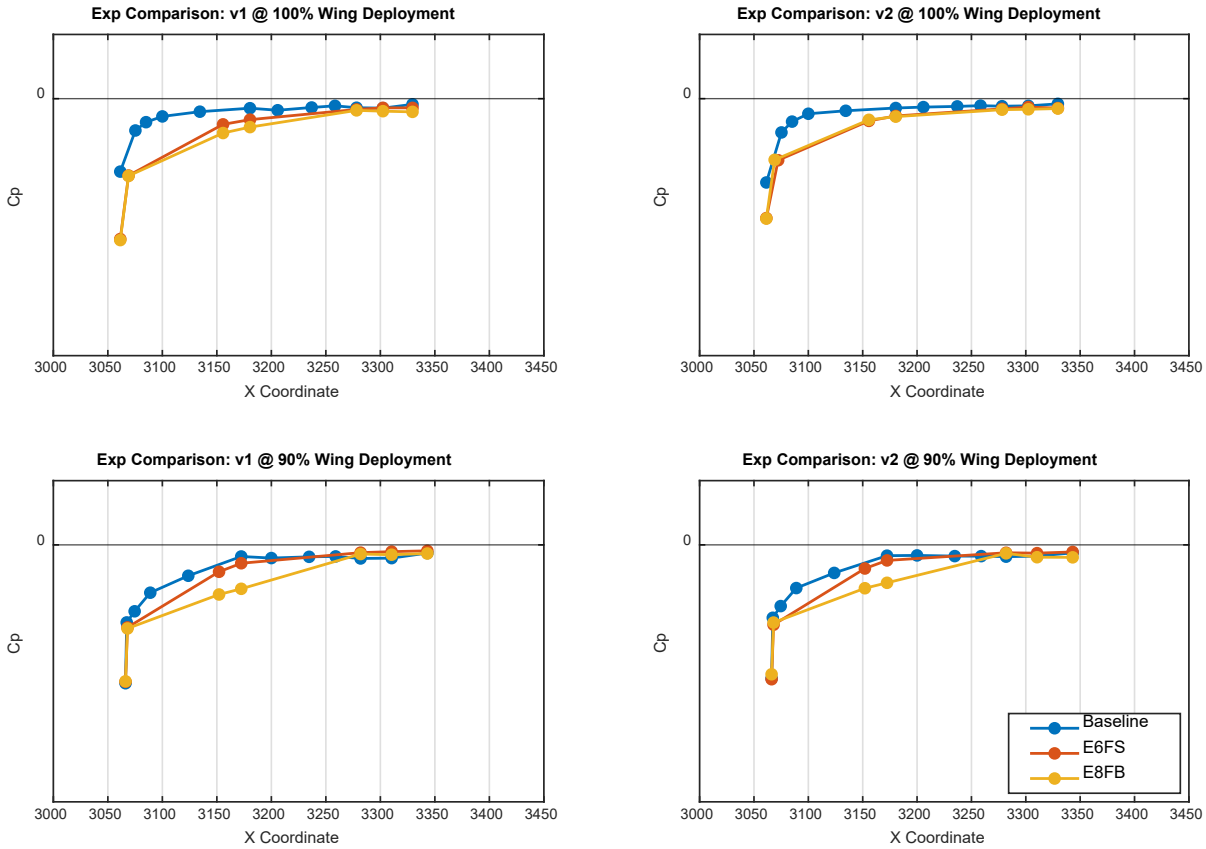


Figure 34. Experimental local pressure coefficient distributions measured on the rear wing section (Section 280 mm) for velocity profiles v1 and v2, comparing the baseline, E6FS, and E8FB configurations at 90% and 100% wing deployment with 100% fan speed.

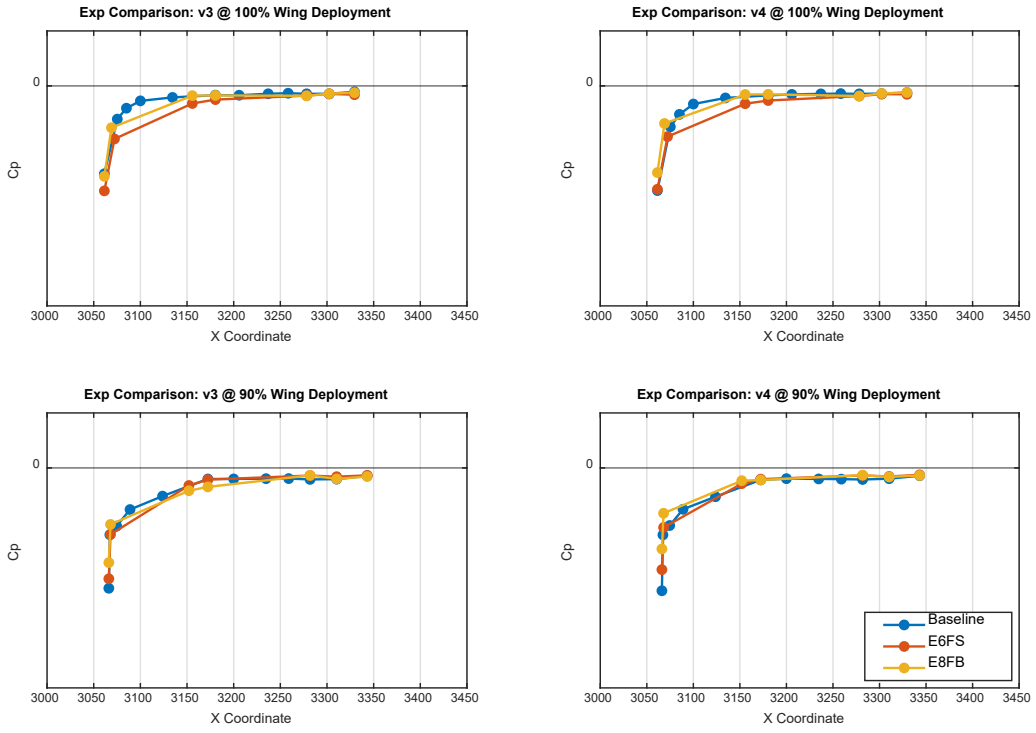


Figure 35. Experimental local pressure coefficient distributions measured on the rear wing section (Section 280 mm) for velocity profiles v3 and v4, comparing the baseline, E6FS, and E8FB configurations at 90% and 100% wing deployment with 100% fan speed.

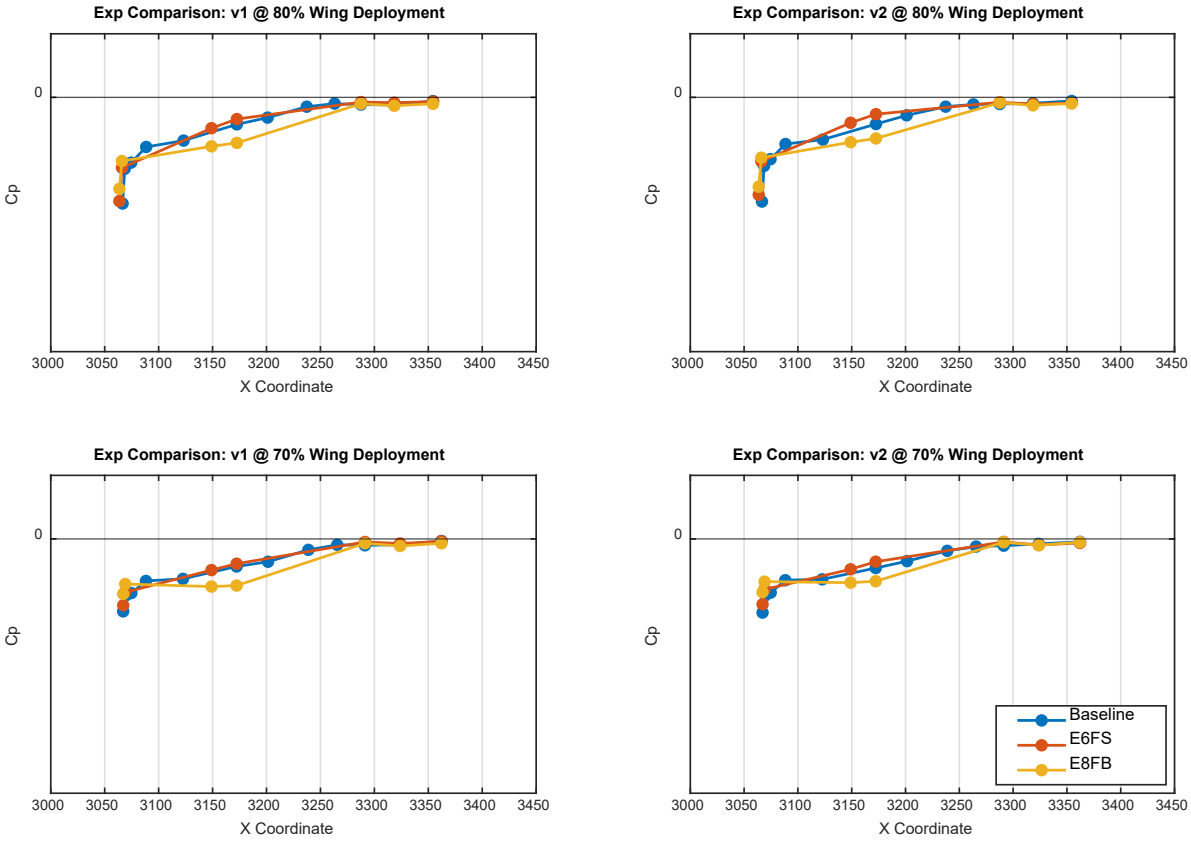


Figure 36. Experimental local pressure coefficient distributions measured on the rear wing section (Section 280 mm) for velocity profiles v1 and v2, comparing the baseline, E6FS, and E8FB configurations at 70% and 80% wing deployment with 100% fan speed.

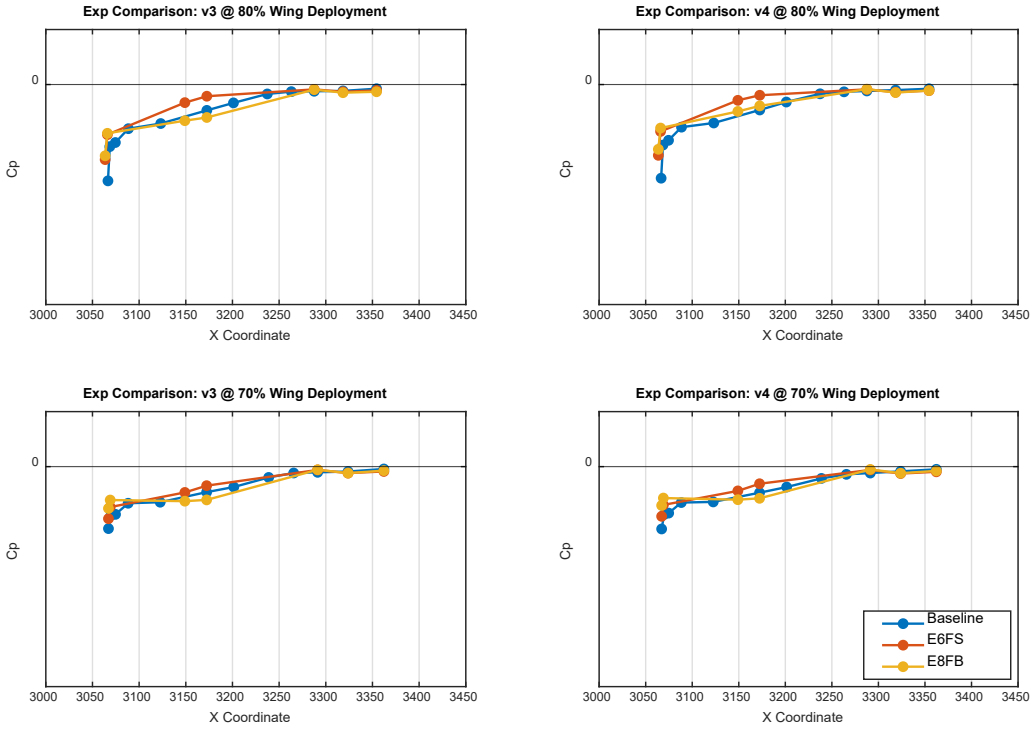


Figure 37. Experimental local pressure coefficient distributions measured on the rear wing section (Section 280 mm) for velocity profiles v3 and v4, comparing the baseline, E6FS, and E8FB configurations at 70% and 80% wing deployment with 100% fan speed.

These observations suggest that the achievable mass flow rate and the resulting momentum coefficient influence the pressure-distribution modifications generated by the Co-Flow system. However, consistent with the lift-coefficient analysis presented previously, the present results indicate that the aerodynamic response cannot be described solely in terms of momentum-coefficient magnitude. Configurations exhibiting similar momentum-coefficient levels may still produce different pressure distributions and different aerodynamic benefits, indicating that the effectiveness of the actuation also depends on the interaction between the injected flow, the local pressure field, and the wing geometry.

To assess the robustness of the experimental campaign, the coefficient of variation (CV) was evaluated for both the aerodynamic measurements and the monitored Co-Flow operating parameters. The resulting global metrics are summarized in Table 8. The low variability observed for the fan operating conditions, control signals, flow-rate measurements, and environmental parameters confirms the stability of the actuation system throughout the test campaign, while the repeatability of the aerodynamic measurements provides confidence in the significance of the reported aerodynamic trends.

Table 8. Global coefficient of variation (CV) metrics for the aerodynamic measurements and monitored Co-Flow operating parameters, calculated across all investigated configurations and operating conditions.

Parameter	Cd	Cl	RPM Fan 1	MFR1	MFR2	P_{elec}	PWM Fan 1	PWM Fan 2	Density
Average CV [%]	1.80%	2.83%	0.01%	3.06%	2.29%	0.76%	0.09%	0.24%	0.12%

The pressure-coefficient measurements were acquired during the same experimental campaign and using the same instrumentation, operating conditions, and data-processing procedures adopted for the vehicle lift-coefficient measurements. Therefore, the repeatability demonstrated by the aerodynamic measurements provides confidence in the robustness of the reported pressure distributions. Furthermore, the pressure-coefficient trends discussed in this section are based on spatially coherent variations observed across multiple pressure taps and repeated operating conditions, reducing the likelihood that the reported effects arise from measurement scatter. Detailed repeatability statistics for the vehicle drag coefficient, vehicle lift coefficient, and monitored Co-Flow operating parameters are reported in Appendix A (Tables A1–A3).

5.4. Efficiency

The energy efficiency of the Co-Flow system was evaluated by comparing the aerodynamic power savings associated with drag reduction against the electrical power consumed by the ducted fans:

$$\eta_{veh} = \frac{\left(Drag_{\,Baseline,veh} - Drag_{CoFlow,veh}\right) \times V_0}{P_{fans}} \tag{14}$$

where $Drag_{Baseline,veh}$ and $Drag_{CoFlow,veh}$ are the measured vehicle drag forces for the baseline and Co-Flow configurations, respectively, P_{fans} is the measured electrical power consumed by the two ducted fans and their associated electronic speed controllers, and V_∞ is the vehicle speed. Values of $\eta > 1$ indicate that the aerodynamic power savings associated with drag reduction exceed the electrical power required by the actuation system.

Although the momentum coefficient C_μ represents the governing aerodynamic parameter of the Co-Flow system and was previously discussed in relation to the lift and pressure-distribution results, it is not explicitly included in Equation (14). The adopted

formulation was intentionally based on directly measured aerodynamic and electrical quantities. In contrast, an explicit formulation in terms of C_μ would require the estimation of additional jet-related quantities, including the effective jet velocity and the corresponding jet power.

The influence of C_μ is nevertheless inherently reflected in both the measured drag reduction and the electrical power required to generate the corresponding momentum injection.

Figures 38–40 summarize the efficiency trends obtained for the investigated Co-Flow configurations as a function of vehicle speed, fan rotational speed, and rear-wing deployment. For all configurations, efficiency generally increases with vehicle speed and wing deployment, indicating that the aerodynamic benefits associated with the Co-Flow system become more significant under highly loaded operating conditions. Conversely, increasing fan speed does not necessarily produce proportional efficiency gains, as the additional aerodynamic benefit may be partially offset by the corresponding increase in electrical power consumption. The E6FS configuration consistently exhibits the lowest efficiency levels throughout the investigated operating range (Figure 38). While positive aerodynamic benefits are observed under several operating conditions, the resulting drag reduction remains relatively modest compared with the electrical power required by the actuation system. Consequently, E6FS provides the least favourable balance between aerodynamic performance and energy expenditure among the investigated solutions.

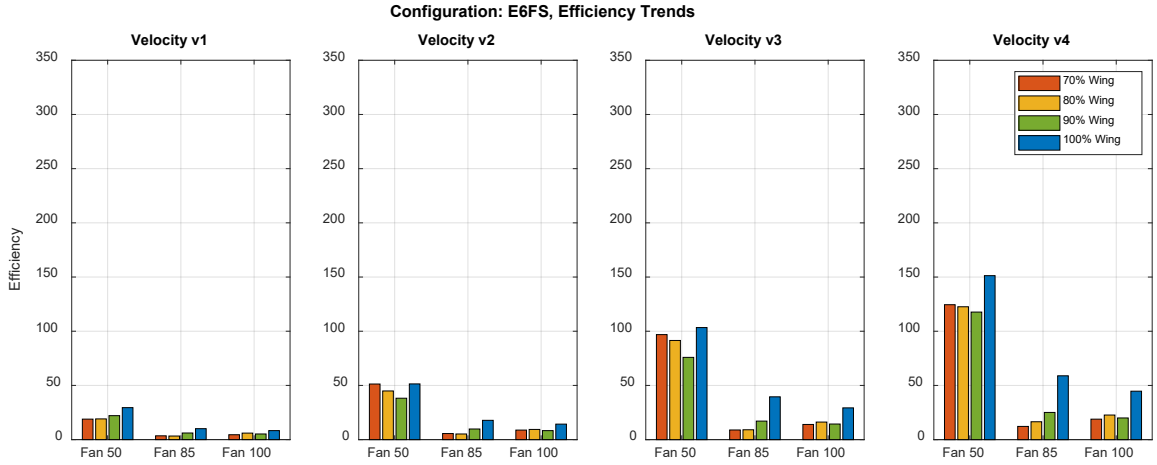


Figure 38. Vehicle-level efficiency trends of the E6FS configuration relative to the baseline case, showing the variation in the efficiency metric derived from the complete vehicle aerodynamic response across velocity profiles, wing deployment positions, and fan operating speeds.

The E8FB configuration achieves the highest efficiency and exhibits the most favourable global behaviour (Figure 39). Efficiency increases substantially with vehicle speed and reaches its highest values at large wing-deployment angles.

The efficiency analysis indicates that the aerodynamic gains obtained with E8FB increase more rapidly than the associated electrical power consumption, resulting in the highest energy-return values of the investigated configurations. The E9aFB configuration also achieves substantial efficiency improvements compared with E6FS, particularly at high vehicle speeds and large wing-deployment angles (Figure 40). However, despite the larger mass-flow capability of this configuration, its efficiency remains generally lower than that achieved by E8FB. This behaviour suggests that the additional momentum injection provided by E9aFB does not translate into proportional aerodynamic benefits over the investigated operating range.

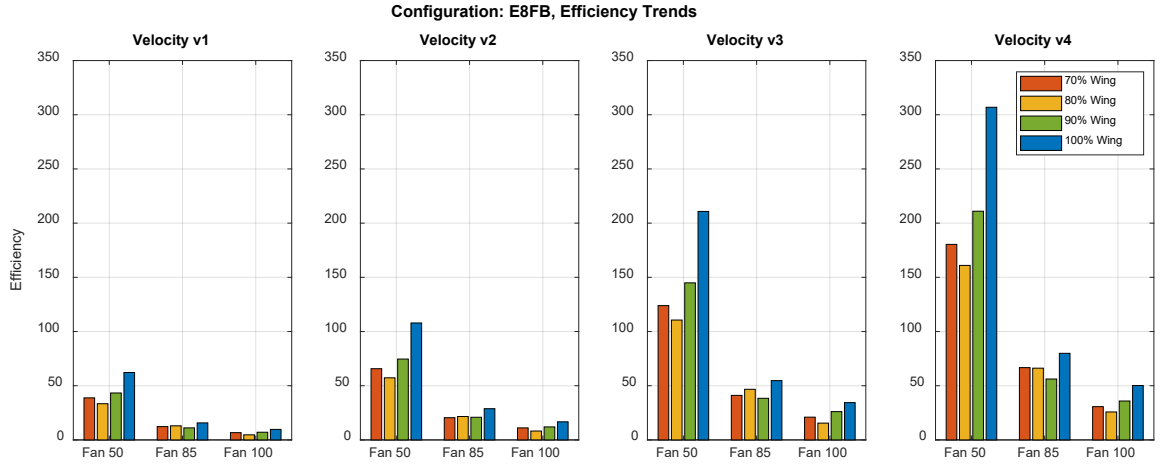


Figure 39. Vehicle-level efficiency trends of the E8FB configuration relative to the baseline case, showing the variation in the efficiency metric derived from the complete vehicle aerodynamic response across velocity profiles, wing deployment positions, and fan operating speeds.

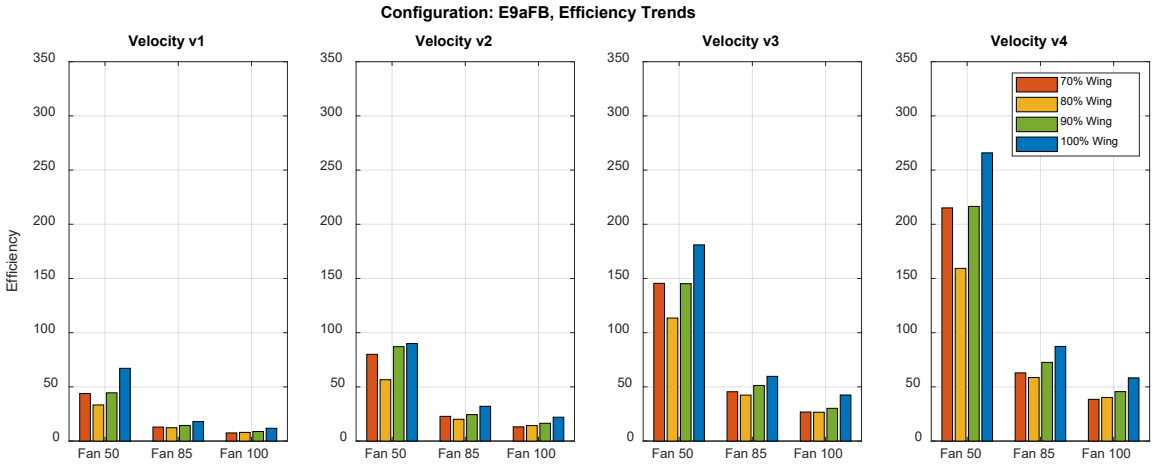


Figure 40. Vehicle-level efficiency trends of the E9aFB configuration relative to the baseline case, showing the variation in the efficiency metric derived from the complete vehicle aerodynamic response across velocity profiles, wing deployment positions, and fan operating speeds.

A direct comparison between E8FB and E9aFB further confirms the superior performance of E8FB. As summarized in Table 9, E8FB achieves higher efficiency than E9aFB in 37 out of the 48 operating conditions investigated.

Although E9aFB outperforms E8FB under a limited number of specific conditions, the ultimate results demonstrate that increasing the available mass flow rate alone is not sufficient to maximize system efficiency. Instead, the aerodynamic effectiveness of the injected momentum and the corresponding electrical power required to generate it must be considered simultaneously. The proposed efficiency metric should therefore be interpreted as an aerodynamic power-balance indicator rather than as a complete vehicle-level energy assessment. Its objective is to quantify the aerodynamic benefit obtained from the Co-Flow system relative to the electrical power required for its operation under representative vehicle operating conditions. The metric provides a practical comparison between different Co-Flow configurations by considering the measured aerodynamic response together with the corresponding electrical power demand of the actuation system. As such, it allows the relative merits of the investigated solutions to be assessed on a common basis and highlights the trade-off between aerodynamic performance and energy expenditure. However, the present analysis does not account for vehicle-level considerations such as

battery sizing, additional system mass, thermal-management requirements, packaging constraints, durability, or long-term operating strategies. These aspects require a dedicated system-integration assessment and are therefore beyond the scope of the present investigation. Consequently, the reported efficiency values should be interpreted as a comparative indicator of aerodynamic effectiveness per unit of electrical power consumed rather than as a prediction of the energy efficiency of a production vehicle.

Table 9. Relative vehicle-level efficiency difference (Δη) between the E8FB and E9aFB configurations for all investigated velocity profiles, wing deployment positions, and fan speeds. Green cells indicate positive efficiency differences (Δη > 0), corresponding to operating conditions where E8FB is more efficient than E9aFB, whereas blue cells indicate negative efficiency differences (Δη < 0), corresponding to conditions favouring E9aFB. The dominance count reports the total number of favourable operating points for each configuration.

Total					
E8FB	**37**	**Delta Efficiency > 0, E8FB > E9aFB**			
E9aFB	**11**				
Veh Speed	% Fan	70	80	90	100
v1	50%	13%	−1%	3%	8%
v1	85%	4%	−6%	29%	14%
v1	100%	12%	69%	23%	22%
v2	50%	22%	−1%	17%	−17%
v2	85%	11%	−7%	17%	12%
v2	100%	18%	73%	37%	32%
v3	50%	17%	3%	0%	−14%
v3	85%	11%	−9%	34%	9%
v3	100%	28%	72%	16%	24%
v4	50%	19%	−1%	3%	−13%
v4	85%	−6%	−11%	29%	9%
v4	100%	26%	56%	27%	16%

6. Conclusions

This work presented a combined numerical and experimental investigation of a fan-driven Co-Flow system integrated within the rear wing of a full-scale high-performance vehicle. The study focused on the aerodynamic response of three Co-Flow configurations (E6FS, E8FB, and E9aFB) under realistic on-track operating conditions, considering pressure distributions, vehicle drag, aerodynamic load, and actuation-system power consumption. The CFD methodology was primarily employed as a comparative design-support tool and was complemented by full-scale experimental testing. The results demonstrated that the flow-control effectiveness of the investigated Co-Flow systems is strongly influenced by duct architecture, operating conditions, and the balance between blowing and suction. Among the tested configurations, E8FB consistently provided the most favourable compromise between aerodynamic effectiveness and power consumption across the investigated operating envelope. The configuration achieved repeatable drag reductions and downforce improvements while maintaining comparatively robust behaviour over a broad range of fan operating conditions. In contrast, E9aFB demonstrated that increasing mass-flow capability alone does not necessarily translate into superior aerodynamic performance. Although this configuration occasionally achieved larger peak benefits, its response was more sensitive to operating conditions and showed a stronger tendency toward diminishing aerodynamic returns at higher actuation levels. Similarly, E6FS exhibited limited effectiveness, particularly

under highly loaded operating conditions, where the front-suction arrangement restricted the achievable flow-control authority. The experimental results further indicate that the aerodynamic benefits obtained from the investigated Co-Flow systems are governed not only by the magnitude of the injected momentum but also by its interaction with the external aerodynamic loading. The pressure-coefficient measurements and aerodynamic-force trends suggest improved pressure recovery for the most effective configurations. However, the underlying flow mechanisms were inferred from the combined interpretation of CFD results and surface-pressure measurements rather than from direct experimental flow-field measurements. The efficiency analysis showed that the best-performing configurations can produce aerodynamic benefits that exceed the electrical power required by the actuation system under selected operating conditions. However, the adopted efficiency metric should be interpreted as an aerodynamic power-balance indicator based on experimentally measured quantities rather than as a complete vehicle-level energy assessment. Additional factors such as battery sizing, system mass, thermal-management requirements, acoustic performance, durability, and long-term operational feasibility were outside the scope of the present study. The present investigation represents a full-scale demonstration of the integration and operation of a fan-driven Co-Flow system on a production-based high-performance vehicle. However, the findings should be interpreted within the limitations of the study. The experimental campaign was conducted on a single vehicle platform; only three Co-Flow configurations were experimentally investigated; the operating-speed range was intentionally restricted; and no dedicated wind-tunnel or wake-survey measurements were available. Furthermore, the mesh-sensitivity analysis was performed on the isolated rear-wing assembly rather than on the complete vehicle, representing a practical compromise between computational cost and numerical assessment during the CFD development process. Due to confidentiality constraints, part of the absolute aerodynamic data could not be disclosed, and the CFD validation relied on vehicle-level aerodynamic metrics and surface-pressure distributions rather than detailed flow-field measurements. Future work should therefore focus on direct experimental characterization of the flow-control mechanisms through velocity-field measurements, wake surveys, or particle image velocimetry, as well as on the investigation of a broader range of geometries and operating conditions. Additional studies addressing acoustic behaviour, durability, packaging constraints, and vehicle-level energy implications will also be required to fully assess the applicability of Co-Flow systems in production automotive environments.

Author Contributions: Conceptualization, M.R.H.; methodology, M.R.H., S.D.P., G.P. and M.D.d.T.; software, M.R.H. and G.L.B.; validation, M.R.H., S.D.P.; formal analysis, M.R.H., G.L.B., G.P. and M.D.d.T.; investigation, M.R.H., G.P. and M.D.d.T.; resources, M.R.H.; data curation, M.R.H. and G.L.B.; writing—original draft preparation, M.R.H.; writing—review and editing, G.P. and M.D.d.T.; visualization, M.R.H.; supervision, S.D.P., G.P. and M.D.d.T. All authors have read and agreed to the published version of the manuscript.

Funding: M. D. de Tullio and G. Pascazio were partially supported by the Italian Ministry of Education, University and Research under the Program Department of Excellence Legge 232/2016 (Grant No. CUP-D93C23000100001).

Institutional Review Board Statement: Not applicable.

Informed Consent Statement: Not applicable.

Data Availability Statement: Data are contained within the article.

Conflicts of Interest: Authors Marco Robert Herberg, Guglielmo Luca Bambino, and Stefano De Pinto were employed by the company McLaren Automotive Europe SL. The remaining authors declare that the research was conducted in the absence of any commercial or financial relationships that could be construed as a potential conflict of interest.

Appendix A. Experimental Repeatability Assessment

To quantify the repeatability of the experimental campaign, the coefficient of variation (CV [%]) was evaluated using repeated acquisitions according to:

$$\mathrm{CV}(C_{X,\mathrm{veh}})[\%] = \frac{\sigma_{CX}}{\mu_{CX}} \times 100 \tag{A1}$$

where σ_{CX} is the standard deviation of the repeated measurements and μ_{CX} is the corresponding mean value. The repeatability assessment was performed separately for the vehicle drag coefficient and the vehicle lift coefficient, since the two quantities were obtained using different experimental procedures. For the drag coefficient, repeatability was evaluated from repeated coastdown measurements performed under identical operating conditions. The resulting coefficient of variation was calculated for each investigated Co-Flow configuration, fan-speed setting, and wing-deployment condition. For the lift coefficient and the monitored Co-Flow operating parameters, repeatability was evaluated from repeated steady-state measurements performed for each combination of vehicle speed, wing-deployment setting, fan rotational speed, and Co-Flow configuration. The resulting CV values were subsequently averaged to provide representative repeatability metrics for each configuration, while the standard deviation of the calculated CV values was used to quantify the variability of the repeatability across the investigated operating envelope. Table A1 reports the detailed repeatability metrics for the vehicle drag coefficient, while Tables A2 and A3 summarize the average coefficient of variation and the corresponding standard deviation obtained for the vehicle lift coefficient and the monitored Co-Flow operating parameters throughout the experimental campaign.

Table A1. Detailed coefficient of variation (CV) of the vehicle drag coefficient, $\mathrm{CV}(C_{d,\mathrm{veh}})$, obtained from repeated coastdown measurements for all investigated Co-Flow configurations, fan-speed settings, and wing-deployment conditions. The average coefficient of variation across the complete experimental campaign was 1.80%, with a standard deviation of 0.70%.

Design	Wing Deployment	FAN RPM [%]	CV(Cd,veh) [%]
E6FS	70%	50%	2.94%
	80%	50%	3.14%
	90%	50%	0.63%
	100%	50%	1.59%
	70%	85%	1.22%
	80%	85%	1.08%
	90%	85%	1.93%
	100%	85%	1.17%
	70%	100%	2.21%
	80%	100%	2.32%
	90%	100%	0.71%
	100%	100%	1.65%

Table A1. *Cont.*

Design	Wing Deployment	FAN RPM [%]	CV(Cd,veh) [%]
E8FB	0%	0%	1.57%
	0%	30%	1.20%
	0%	50%	0.89%
	70%	50%	2.36%
	80%	50%	1.05%
	90%	50%	2.77%
	100%	50%	0.88%
	70%	85%	1.33%
	80%	85%	2.71%
	90%	85%	0.79%
	100%	85%	1.78%
	70%	100%	2.92%
	80%	100%	1.63%
	90%	100%	1.61%
	100%	100%	2.68%
E9aFB	0%	0%	2.04%
	0%	30%	2.13%
	0%	50%	1.64%
	70%	50%	1.50%
	80%	50%	1.55%
	90%	50%	2.35%
	100%	50%	1.86%
	70%	85%	2.86%
	80%	85%	1.57%
	90%	85%	1.35%
	100%	85%	1.87%
	70%	100%	1.61%
	80%	100%	1.51%
	90%	100%	1.69%
	100%	100%	3.40%

Table A2. Average coefficient of variation (CV) of the vehicle lift coefficient, $CV_{(Cl,veh)}$, and of the monitored Co-Flow operating parameters, evaluated from repeated steady-state measurements for all investigated Co-Flow configurations and fan-speed settings. The reported values correspond to the mean CV calculated across the investigated vehicle-speed and wing-deployment conditions.

Design	Fan	Parameter	C_l	RPM Fan 1	MFR1	MFR2	P_{elec}	PWM Fan 1	PWM Fan 2	Density
E6FS	50%	Average CV [%]	3.00%	0.00%	3.97%	4.04%	0.83%	0.05%	0.22%	0.18%
	85%	Average CV [%]	4.51%	0.01%	1.27%	1.54%	1.46%	0.15%	0.51%	0.16%
	100%	Average CV [%]	3.70%	0.01%	1.96%	1.97%	1.39%	0.17%	0.59%	0.08%

Table A2. *Cont.*

Design	Fan	Parameter	C_l	RPM Fan 1	MFR1	MFR2	P_{elec}	PWM Fan 1	PWM Fan 2	Density
E8FB	50%	Average CV [%]	2.16%	0.00%	4.20%	2.69%	0.21%	0.01%	0.03%	0.08%
	85%	Average CV [%]	3.28%	0.02%	8.48%	3.93%	0.54%	0.11%	0.14%	0.15%
	100%	Average CV [%]	1.90%	0.00%	5.47%	3.34%	0.48%	0.08%	0.18%	0.09%
E9aFB	50%	Average CV [%]	1.48%	0.00%	0.68%	1.06%	0.54%	0.03%	0.12%	0.06%
	85%	Average CV [%]	2.82%	0.02%	0.75%	1.17%	0.71%	0.13%	0.19%	0.22%
	100%	Average CV [%]	2.63%	0.01%	0.76%	0.90%	0.64%	0.09%	0.19%	0.08%

Table A3. Standard deviation of the coefficient of variation (CV) of the vehicle lift coefficient, $CV(C_{l,veh})$, and of the monitored Co-Flow operating parameters, evaluated from repeated steady-state measurements for all investigated Co-Flow configurations and fan-speed settings. The reported values quantify the variability of the repeatability across the investigated vehicle-speed and wing-deployment conditions.

Design	Fan	Parameter	C_l	RPM Fan 1	MFR1	MFR2	P_{elec}	PWM Fan 1	PWM Fan 2	Density
E6FS	50%	CV Std. Dev. [%]	2.05%	0.00%	5.78%	6.22%	0.53%	0.03%	0.16%	0.37%
	85%	CV Std. Dev. [%]	2.41%	0.02%	0.79%	1.34%	1.21%	0.07%	0.66%	0.10%
	100%	CV Std. Dev. [%]	2.01%	0.01%	3.09%	3.42%	2.32%	0.14%	1.03%	0.07%
E8FB	50%	CV Std. Dev. [%]	3.00%	0.00%	6.97%	7.60%	0.31%	0.02%	0.03%	0.12%
	85%	CV Std. Dev. [%]	1.48%	0.02%	7.56%	4.54%	0.68%	0.09%	0.10%	0.17%
	100%	CV Std. Dev. [%]	1.27%	0.01%	3.53%	2.62%	0.35%	0.06%	0.12%	0.21%
E9aFB	50%	CV Std. Dev. [%]	0.76%	0.00%	0.70%	1.31%	0.54%	0.02%	0.13%	0.08%
	85%	CV Std. Dev. [%]	1.21%	0.02%	0.67%	1.75%	0.71%	0.09%	0.18%	0.25%
	100%	CV Std. Dev. [%]	1.31%	0.01%	0.61%	1.31%	0.60%	0.06%	0.09%	0.10%

References

1. Connolly, M.G.; Ivankovic, A.; O'Rourke, M.J. Drag reduction technology and devices for road vehicles: A comprehensive review. *Heliyon* **2024**, *10*, e33757. [CrossRef] [PubMed]
2. Katz, J. Aerodynamics in motorsports. *Proc. Inst. Mech. Eng. Part P J. Sports Eng. Technol.* **2021**, *235*, 324–338. [CrossRef]
3. Liu, H. Racing car aerodynamics: Optimising vehicle drag reduction and downforce control. In *Proceedings of the 2025 2nd International Conference on Electrical Engineering and Intelligent Control (EEIC 2025)*; Springer: Berlin/Heidelberg, Germany, 2025; pp. 837–847. [CrossRef] [PubMed]
4. Sudin, M.N.; Abdullah, M.; Shamsudin, S.; Faiz, R.; Tahir, M. Review of research on vehicles aerodynamic drag reduction methods. *Int. J. Mech. Mechatron. Eng.* **2014**, *14*, 35–47.
5. Ravelli, U.; Ravelli, S. An overview of drag reduction methods in road cars. *Fluid Dyn. Mater. Process.* **2026**, *22*, 1. [CrossRef]
6. Agarwal, A.; Mthembu, L. Computational analysis for enhancing motorcycle aerodynamics by modifying engine bay openings. *J. Eur. Syst. Autom.* **2025**, *58*, 1079–1087. [CrossRef]
7. Marumo, R.; Molwane, O.B.; Agarwal, A. Numerical Analysis of Rear Spoilers in Improving Vehicle Traction. In *Advances in Lightweight Materials and Structures; Springer Proceedings in Materials*; Springer: Singapore, 2020; Volume 8. [CrossRef]
8. Piechna, J. A review of active aerodynamic systems for road vehicles. *Energies* **2021**, *14*, 7887. [CrossRef]
9. Gad-el-Hak, M. *Flow Control: Passive, Active, and Reactive Flow Management*; Cambridge University Press: Cambridge, UK, 2000.
10. Cattafesta, L.N.; Sheplak, M. Actuators for active flow control. *Annu. Rev. Fluid Mech.* **2011**, *43*, 247–272. [CrossRef]
11. Ramadhan, R.D.R.; Mat, S.; Samin, P.M.; Othman, N.; Wahid, M.A. Review on flow controls for vehicles aerodynamic drag reduction. *J. Adv. Res. Fluid Mech. Therm. Sci.* **2023**, *101*, 11–36. [CrossRef]
12. Herberg, M.R.; De Pinto, S.; de Tullio, M.D.; Pascazio, G. Active flow control techniques: Classification, analysis, and future trends for automotive applications. *Fluids* **2026**, *11*, 106. [CrossRef]
13. Ho, H.H.; Shirinzad, A.; Essel, E.E.; Sullivan, P.E. Synthetic jet actuators for active flow control: A review. *Fluids* **2024**, *9*, 290. [CrossRef]

14. Modi, V.J.; Fernando, M.S.U.K.; Yokomizo, T. Moving surface boundary-layer control: Studies with bluff bodies and application. *AIAA J.* **1991**, *29*, 1400–1406. [CrossRef] [PubMed]
15. Brunn, A.; Wassen, E.; Sperber, D.; Nitsche, W.; Thiele, F. Active drag control for a generic car model. In *Proceedings of the Active Flow Control 2006, Berlin, Germany, 27–29 September 2006*; Springer: Berlin/Heidelberg, Germany, 2007; pp. 247–259. [CrossRef]
16. Jahanmiri, M. *Active Flow Control: A Review*; Chalmers University of Technology: Göteborg, Sweden, 2010.
17. Piechna, J.; Kurec, K.; Broniszewski, J.; Remer, M.; Piechna, A.; Kamieniecki, K.; Bibik, P. Influence of the car movable aerodynamic elements on fast road car cornering. *Energies* **2022**, *15*, 689. [CrossRef]
18. Ahmed, S.R.; Ramm, G.; Faltin, G. Some salient features of the time-averaged ground vehicle wake. *SAE Trans.* **1984**, *93*, 473–503. [CrossRef]
19. Maine, M.; Oumami, E.M.; Bouksour, O.; Tizliouine, A. Review of research on cars wake flow control methods to reduce aerodynamic drag. *Int. J. Innov. Appl. Stud.* **2019**, *25*, 1069–1089.
20. Rouméas, M.; Gilliéron, P.; Kourta, A. Drag reduction by flow separation control on a car after body. *Int. J. Numer. Methods Fluids* **2009**, *60*, 1222–1240. [CrossRef]
21. Harinaldi, H.; Budiarso, B.; Warjito, W.; Kosasih, E.A.; Tarakka, R.; Simanungkalit, S.P.; Teryanto, L.; Fredy, I.G.M. Modification of flow structure over a van model by suction flow control to reduce aerodynamic drag. *Makara J. Technol.* **2012**, *16*, 3. [CrossRef]
22. Phan, T.-L.; Pham, Q.T.; Nguyen, T.K.L.; Nguyen, T.T. A numerical analysis of active flow control techniques for aerodynamic drag reduction in the square-back Ahmed model. *Appl. Sci.* **2023**, *13*, 239. [CrossRef]
23. Mukuk, M.I.; Abedin, M.Z. Review on aerodynamic drag reduction of vehicles. *Int. J. Eng. Mater. Manuf.* **2019**, *4*, 1–14. [CrossRef]
24. Zha, G.; Paxton, C. A novel airfoil circulation augment flow control method using co-flow jet. In Proceedings of the 2nd AIAA Flow Control Conference, Portland, OR, USA, 28–30 June 2004. [CrossRef]
25. Zha, G.; Carroll, B.; Paxton, C.; Conley, C.; Wells, A. High-performance airfoil using co-flow jet flow control. *AIAA J.* **2007**, *45*, 2087–2090. [CrossRef]
26. Zha, G.; Gao, W.; Paxton, C. Jet effects on co-flow jet airfoil performance. *AIAA J.* **2007**, *45*, 1222–1231. [CrossRef]
27. Lefebvre, A.; Dano, B.; Bartow, W.; Difronzo, M.; Zha, G. Performance and energy expenditure of co-flow jet airfoil with variation of Mach number. *J. Aircr.* **2016**, *53*, 1757–1767. [CrossRef]
28. Zhi, H.; Zhu, Z.; Lu, Y.; Deng, S.; Xiao, T. Aerodynamic performance enhancement of co-flow jet airfoil with simple high-lift device. *Chin. J. Aeronaut.* **2021**, *34*, 143–155. [CrossRef]
29. Zhu, Z.; Xiao, T.; Zhi, H.; Deng, S.; Lu, Y. Aerodynamic characteristics of co-flow jet wing with simple high-lift devices. *Chin. J. Aeronaut.* **2022**, *35*, 67–83. [CrossRef]
30. Vigneswaran, C.; Kumar, G.C.V. Aerodynamic performance analysis of co-flow jet airfoil. *Int. J. Aviat. Aeronaut. Aerosp.* **2021**, *8*, 10. [CrossRef]
31. Dano, B.P.E.; Kirk, D.; Zha, G.-C. Experimental investigation of jet mixing of a co-flow jet airfoil. In Proceedings of the 5th AIAA Flow Control Conference, Chicago, IL, USA, 28 June–1 July 2010. [CrossRef]
32. Derghal, I.; Mohd Saifuddin, M.; Mohd Noh, M.H.; Abdul Hamid, A.H. Optimization of co-flow jet parameters for Ahmed body application. *Int. J. Integr. Eng.* **2023**, *15*, 233–243. [CrossRef]
33. Jahanmiri, M.; Abbaspour, M. Experimental investigation of drag reduction on Ahmed car model using a combination of active flow control methods. *Int. J. Eng.* **2011**, *24*, 403–410. [CrossRef]
34. Agarwal, A.; Mthembu, L. CFD analysis of conical diffuser under swirl flow inlet conditions using turbulence models. *Mater. Today Proc.* **2020**, *27*, 1350–1355. [CrossRef]
35. Segers, J. *Analysis Techniques for Racecar Data Acquisition*, 2nd ed.; Segers Aero Corporation: Indianapolis, IN, USA, 2014.
36. *ISO 5801:2017*; Industrial Fans—Performance Testing Using Standardized Airways. International Organization for Standardization (ISO): Geneva, Switzerland, 2017.
37. John, J.E.A.; Haberman, W.L. *Introduction to Fluid Mechanics*, 3rd ed.; McGraw-Hill: New York, NY, USA, 1988.
38. Miller, D.S. *Internal Flow Systems*, 2nd ed.; BHRA: Cranfield, UK, 1990.
39. Vector Informatik GmbH. *CANape Testing Software*, version 17.0; Computer Software; Vector Informatik GmbH: Stuttgart, Germany, 2021.

Disclaimer/Publisher's Note: The statements, opinions and data contained in all publications are solely those of the individual author(s) and contributor(s) and not of MDPI and/or the editor(s). MDPI and/or the editor(s) disclaim responsibility for any injury to people or property resulting from any ideas, methods, instructions or products referred to in the content.